



<http://www.diva-portal.org>

This is the published version of a paper published in *Geochemistry Geophysics Geosystems*.

Citation for the original published paper (version of record):

Bailey, L R., Drake, H., Whitehouse, M J., Reiners, P W. (2022)
Characteristics and Consequences of Red Bed Bleaching by Hydrocarbon Migration: A
Natural Example From the Entrada Sandstone, Southern Utah
Geochemistry Geophysics Geosystems, 23(8): e2022GC010465
<https://doi.org/10.1029/2022GC010465>

Access to the published version may require subscription.

N.B. When citing this work, cite the original published paper.

Permanent link to this version:

<http://urn.kb.se/resolve?urn=urn:nbn:se:lnu:diva-116362>

Geochemistry, Geophysics, Geosystems®

RESEARCH ARTICLE

10.1029/2022GC010465

Key Points:

- The studied bleached section of Jurassic sandstones in the Paradox Basin reflects interaction with migrating hydrocarbons
- Abundant bitumen supports reduction by hydrocarbons that redistributed iron and high-field strength elements into localized concretions
- Compositional and mineralogical gradients across the bleached sandstone compare well with a batch geochemical model of hydrocarbon migration

Correspondence to:

H. Drake,
Henrik.drake@lnu.se

Citation:

Bailey, L. R., Drake, H., Whitehouse, M. J., & Reiners, P. W. (2022). Characteristics and consequences of red bed bleaching by hydrocarbon migration: A natural example from the Entrada sandstone, southern Utah. *Geochemistry, Geophysics, Geosystems*, 23, e2022GC010465. <https://doi.org/10.1029/2022GC010465>

Received 4 APR 2022

Accepted 11 JUL 2022



Author Contributions:

Conceptualization: Peter W. Reiners
Data curation: Lydia R. Bailey, Henrik Drake, Martin J. Whitehouse
Formal analysis: Lydia R. Bailey, Henrik Drake, Martin J. Whitehouse
Funding acquisition: Peter W. Reiners
Investigation: Lydia R. Bailey, Henrik Drake, Martin J. Whitehouse, Peter W. Reiners
Methodology: Lydia R. Bailey, Peter W. Reiners
Project Administration: Peter W. Reiners
Software: Lydia R. Bailey
Supervision: Peter W. Reiners
Visualization: Lydia R. Bailey

© 2022. The Authors.

This is an open access article under the terms of the [Creative Commons Attribution License](#), which permits use, distribution and reproduction in any medium, provided the original work is properly cited.

Characteristics and Consequences of Red Bed Bleaching by Hydrocarbon Migration: A Natural Example From the Entrada Sandstone, Southern Utah

Lydia R. Bailey¹ , Henrik Drake², Martin J. Whitehouse³, and Peter W. Reiners^{1,4} 

¹Department of Geosciences, University of Arizona, Tucson, AZ, USA, ²Department of Biology and Environmental Science, Linnæus University, Kalmar, Sweden, ³Department of Geosciences, Swedish Museum of Natural History, Stockholm, Sweden, ⁴Faculty of Environment, University of Northern British Columbia, Prince George, BC, Canada

Abstract Extensive regions of yellow and white (“bleached”) sandstones within the terrestrial Jurassic red bed deposits of the Colorado Plateau reflect widespread interaction with subsurface reduced fluids which resulted in the dissolution of iron-oxide grain coatings. Reduced fluids such as hydrocarbons, CO₂, and organic acids have been proposed as bleaching agents. In this study, we characterize an altered section of the Slick Rock member of the Jurassic Entrada Sandstone that exposes bleached sandstone with bitumen-saturated pore spaces. We observe differences in texture, porosity, mineralogy, and geochemistry between red, pink, yellow, and gray facies. In the bleached yellow facies we observe quartz overgrowths, partially dissolved K-feldspar, calcite cement, fine-grained illite, TiO₂-minerals, and pyrite concretions. Clay mineral content is highest at the margins of the bleached section. Fe₂O₃ concentrations are reduced up to 3× from the red to gray facies but enriched up to 50× in iron-oxide concretions. Metals such as Zn, Pb, and rare-earth elements are significantly enriched in the concretions. Supported by a batch geochemical model, we conclude the interaction of red sandstones with reduced hydrocarbon-bearing fluids caused iron-oxide and K-feldspar dissolution, and precipitation of quartz, calcite, clay, and pyrite. Localized redistribution of iron into concretions can account for most of the iron removed during bleaching. Pyrite and carbonate stable isotopic data suggest the hydrocarbons were sourced from the Pennsylvanian Paradox Formation. Bitumen in pore spaces and pyrite precipitation formed a reductant trap required to produce Cu, U, and V enrichment in all altered facies by younger, oxidized saline brines.

Plain Language Summary Thin coatings of iron-oxide on grains give sandstones deposited during the Jurassic Period on the Colorado Plateau a characteristic red pigment. Vast areas of yellow and white (“bleached”) colored sandstones within these red bed deposits represent widespread interaction with fluids such as hydrocarbons, carbon dioxide, and organic acids, which dissolved the iron-oxide grain coatings. These altered sandstones can provide useful information on hydrocarbons or carbon dioxide plume migration pathways, relevant to long-term geological storage of carbon dioxide. In this study, we characterize a section of the Jurassic Entrada Sandstone that exposes a bleached sandstone with hydrocarbon-saturated pore spaces. By comparing the unaltered red sandstones to the bleached sandstones at the study site, we find that hydrocarbon-bearing fluids dissolved minerals like iron-oxide and K-feldspar, and precipitated minerals such as quartz, calcite, clay, and pyrite. The iron that was dissolved has been locally redistributed into small, dense spherical accumulations (concretions) of pyrite and iron-oxide. These accumulations also contain significant enrichment of other metals such as lead, zinc, and rare-earth elements compared to the sandstones. The presence of pyrite and hydrocarbons caused enrichment of copper, uranium, and vanadium in all altered sandstone and concretions compared to the unaltered red sandstone by the later flow of oxidized saline brines.

1. Introduction

Extensive regions of bleached and chemically altered sandstone within the terrestrial red bed deposits of the Colorado Plateau reflect widespread interaction with subsurface reduced fluids (e.g., Beitler et al., 2003; Chan et al., 2000; Loope & Kettler, 2015; Loope et al., 2010). The original characteristic red coloring of these red beds is due to iron-oxide grain coatings formed by breakdown of ferromagnesian silicate minerals during early diagenesis (Walker et al., 1981). Reaction of the red sandstones with reduced aqueous fluids or hydrocarbons causes dissolution of the iron-oxides by reduction to Fe²⁺, resulting in white or yellow “bleached” sandstones.

Writing – original draft: Lydia R. Bailey, Peter W. Reiners
Writing – review & editing: Henrik Drake, Peter W. Reiners

Several studies have shown that iron from the iron-bearing reduced fluids can be locally reprecipitated as disseminated cement or concentrated concretions of pyrite, iron-rich carbonate, or iron-oxides, depending on local conditions. Regardless of their original form, in most cases, these secondary precipitates are present as iron-oxides in surface outcrops, due to interaction with oxidized groundwater (e.g., Beitler et al., 2005; Chan et al., 2007; Gorenc & Chan, 2015). Alternatively, iron dissolved by migrating fluids can remain in solution and be transported with the fluids and ultimately precipitated at redox fronts in other locations, as interpreted for regions of dense Fe-oxide cement and fracture fill (e.g., Chan et al., 2000, 2001; Garcia et al., 2018; Loope et al., 2011; Potter-McIntyre et al., 2013). The distribution of bleaching and iron concretions in sandstones such as the Navajo, White Rim, and Entrada Sandstones have been interpreted as an indicator for the movement of reduced fluids such as hydrocarbons (bitumen), CO₂ and H₂S (Beitler et al., 2005; Chan et al., 2000; Garden et al., 2001; Gorenc & Chan, 2015; Loope et al., 2010; Wigley et al., 2012). However, bitumen is rarely documented in the studied bleached sandstones, and in many cases, there is no direct evidence favoring petroleum versus CO₂, CH₄, H₂S, or another bleaching agent. In our study area bitumen is present in pore spaces of sandstone between two adjacent bleached horizons, so we can directly observe the results of interactions between hydrocarbons and oxidized sandstones. Further insight into the complex history of physical and chemical alteration of red sandstones can provide useful information on hydrocarbon or CO₂ plume migration pathways.

Here, we characterize the sandstones and associated concretions of a section of the Slick Rock member of the Jurassic Entrada Sandstone that exposes bitumen-bearing, altered, and unaltered sandstone in a single outcrop (Chan et al., 2000). The exposure provides an opportunity to study the changes in mineralogic and major- and trace-element proportions, isotopic and mineralogic compositions, and physical properties such as porosity that occur from the interaction of red sandstones and hydrocarbons. Our data show that major, minor, and trace-element concentrations (including “immobile” high-field strength elements) vary by up to, and sometimes over, an order of magnitude from the red, unaltered sandstone to the bitumen-bearing, bleached sandstone. Our mineralogic modal proportions show that minerals such as K-feldspar and iron-oxide decrease in abundance, and illite and quartz increase, from the red to bleached sandstones. We confirm that hydrocarbon migration was accompanied by extensive mobilization of iron and other major and trace elements. Our study has implications for understanding long-term geochemical, mineralogic, and porosity modifications that can impact CO₂ storage capabilities in reservoir sandstones.

2. Geological Setting and Methods

The study site, referred to as Rainbow Rocks by Chan et al. (2000), is in the central Paradox Basin approximately 25 km northwest of Moab, Utah. The studied section is within the Slick Rock member of the Jurassic Entrada Sandstone. We collected 19 variably colored sandstone samples and seven concretion (iron-oxide and carbonate) samples across 30 m of vertical stratigraphic exposure from above to below the bleached and altered section (Figures 1 and 2), with a sample spacing of 0.2–4 m.

We used standard optical microscopy and secondary electron microscopy to describe the modal mineralogy and textures of each sample. Framework and pore-filling mineralogy of representative thin sections for each facies (red, upper pink, lower pink, upper yellow, lower yellow, and gray) was calculated using the Gazzi Dickinson point counting method; 450 points were counted in each thin section, six thin sections in total (Dickinson, 1970, 1988; Ingersoll et al., 1984). We used X-ray fluorescence and inductively coupled plasma mass spectrometry (ICP-MS) on powdered whole rock samples to determine the major, minor, and trace elemental compositions, following the methods described in Johnson et al. (1999).

Pyrite collected from the bitumen-bearing sandstone, and barite from the red sandstone, were analyzed for sulfur isotopes (and oxygen, where applicable). We used the Cameca IMS1280 secondary ion mass spectrometer at the NordSIMS facility. Intra-crystal SIMS-analysis (10 μm lateral beam dimension, 1–2 μm depth dimension) of sulfur isotopes in pyrite was performed on a Cameca IMS1280 ion microprobe at the NordSIM facility at the Museum of Natural History, Stockholm, Sweden, following the analytical settings and tuning reported previously (Drake et al., 2015, 2018; Kamber & Whitehouse, 2007). Sulfur was sputtered using a ¹³³Cs + primary beam with 20 kV incident energy (10 kV primary, −10 kV secondary) and a primary beam current of ~1.5 nA. A normal incidence electron gun was used for charge compensation. Analyses were performed in automated sequences, with each analysis comprising a 70 s pre-sputter to remove the gold coating over a rastered 15 × 15 μm area,

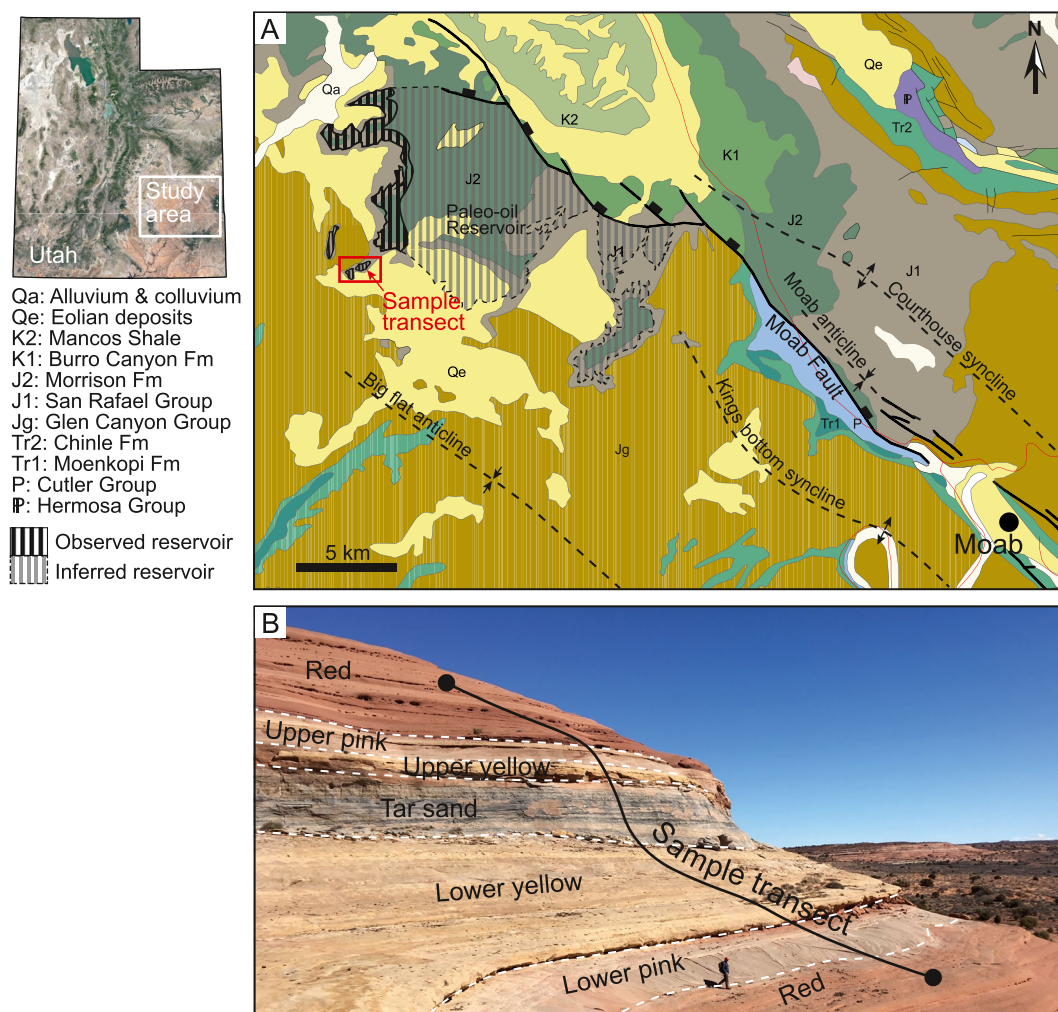


Figure 1. (a) Geologic map of the study area showing the observed and inferred areal extent of the paleo-oil reservoir. The reservoir location is inferred where outcrop was inaccessible, obscured by desert varnish, or in the subsurface (close to the fault zone) (b) outcrop photograph showing sample transect and sandstone facies. The red sandstone extends by at least 40 m above and below the paleo-oil reservoir. Map adapted from Hintze et al. (2000).

centering of the secondary beam in the field aperture to correct for small variations in surface relief, and data acquisition in 16 4-s integration cycles. The magnetic field was locked at the beginning of the session using a nuclear magnetic resonance (NMR) field sensor. Secondary ion signals for ^{32}S and ^{34}S were detected simultaneously using two F detectors with a common mass resolution of 4,860 ($M/\Delta M$). Data were normalized for instrumental mass fractionation using matrix matched reference materials which were mounted together with the sample mounts and analyzed after every sixth sample analysis. Results are reported as per mil (‰) $\delta^{34}\text{S}$ based on the V-CDT reference value (Ding et al., 2001). The pyrite reference material S0302A with a conventionally determined value of $0.0\text{‰} \pm 0.2\text{‰}$ (R. Stern, University of Alberta, personal communication) was used. Typical precision on a single $\delta^{34}\text{S}$ value, after propagating the within run and external uncertainties from the reference material measurements was $\pm 0.07\text{‰}$.

Stable S and O isotopes in barite were also determined within single crystals using the same Cameca IMS1280 SIMS as above. Separate analytical routines applied for S and O, are described briefly below, and closely follow those described by Whitehouse (2013) for sulfur, with the exception that only $^{34}\text{S}/^{32}\text{S}$ ratios were measured here, and Heinonen et al. (2015) for oxygen. For both elements, the samples were sputtered using a Gaussian focused $^{133}\text{Cs}^+$ primary beam with 20 kV incident energy (10 kV primary and -10 kV secondary) and primary beam current of ~ 3 nA, which was rastered over a $5 \times 5 \mu\text{m}$ area during analysis to homogenize the beam density.

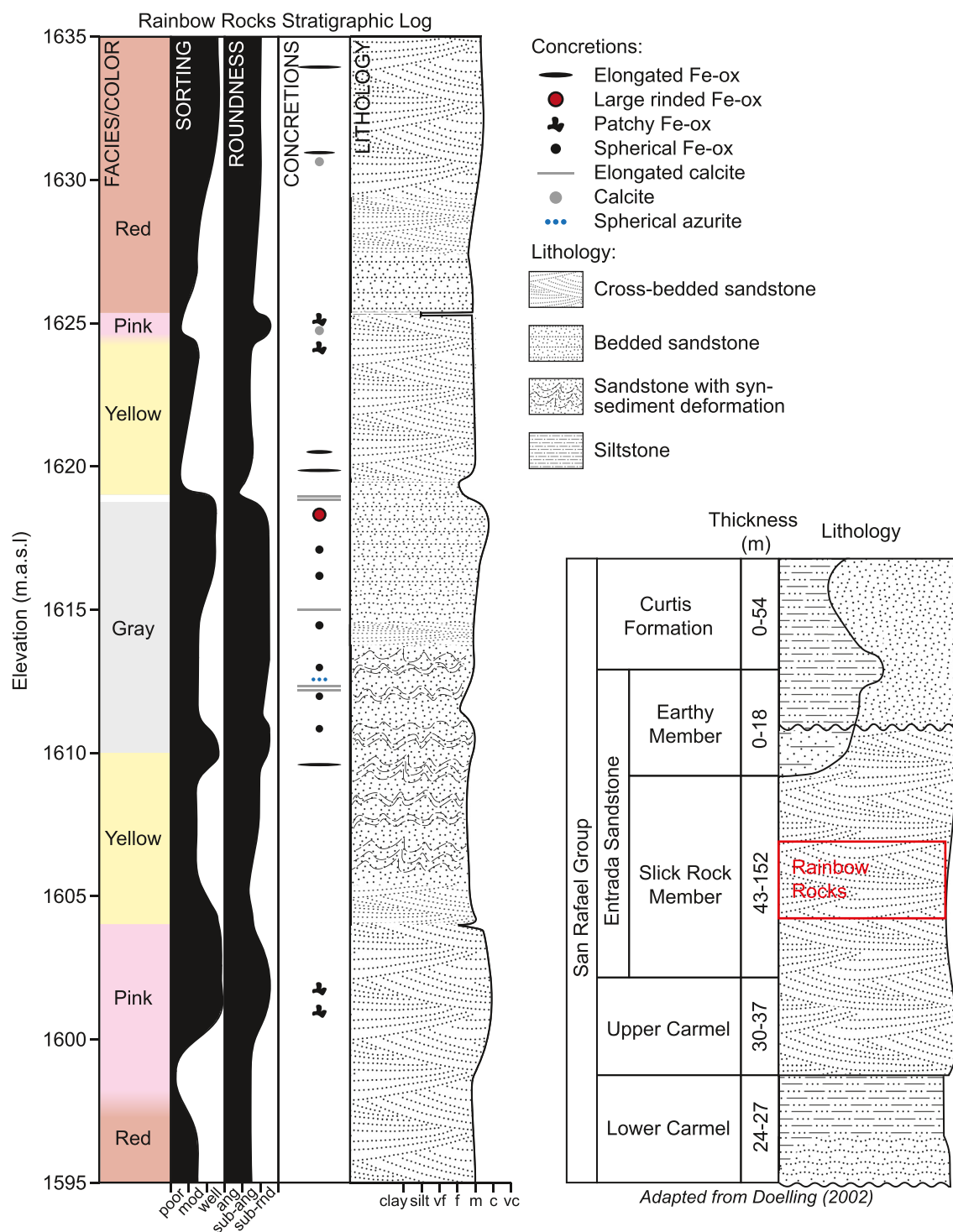


Figure 2. Stratigraphic log of the studied section showing facies/color, sorting (poor, moderate, and well-sorted), grain roundness (ang = angular; sub-ang = sub-angular; and sub-rnd = sub-rounded), concretions, lithology, and bedding. The section is placed in the overall context of the San Rafael Group (Doelling, 2002).

The resulting analytical crater had a diameter of $\sim 10 \mu\text{m}$. A normal incidence electron gun was used for charge compensation. Analyses were performed in automated sequences, with each analysis comprising a 40 s presputter to remove the gold coating over a rastered $15 \times 15 \mu\text{m}$ area, centering of the secondary beam in the field aperture to correct for small variations in surface relief, and data acquisition in 12 4-s integration cycles. The magnetic

Table 1
Petrographic Volume % Compositions From Point-Count Data

Facies	% F Quartz	% F K-spar	% F Plag	% F Other	% S Calcite	% S Fe-ox coatings	% S Fe-concretion	% S Clay	% S Bitumen
Red	75.3	7.3	1.3	0.0	2.4	6.4	2.9	4.2	0.0
Upper pink	62.7	5.6	1.1	0.2	18.2	5.1	3.1	4.0	0.0
Upper yellow	70.2	6.9	1.8	1.3	4.9	0.0	3.1	11.8	0.0
Gray	70.7	4.0	0.2	0.2	3.1	0.0	0.0	2.2	19.6
Lower yellow	71.8	8.9	0.2	0.4	3.8	0.4	2.4	12.0	0.0
Lower pink	73.6	7.8	0.9	0.0	7.8	4.2	0.7	5.1	0.0

Note. 450 points counted at 0.7 mm spacing. F = framework/detrital grains and S = secondary/pore-filling minerals.

field was locked at the beginning of the session using an NMR field sensor. Secondary ion signals (^{32}S and ^{34}S or ^{16}O and ^{18}O) were detected simultaneously using two F detectors with a common mass resolution of 4,860 ($M/\Delta M$) for S and 2,430 ($M/\Delta M$) for O. For barite, the S0327 reference material, with a conventionally determined $\delta^{34}\text{SCDT}$ value of $22.0\text{‰} \pm 0.3\text{‰}$ and $\delta^{34}\text{SCDT}$ value of $11.0\text{‰} \pm 0.1\text{‰}$ (Liseroudi et al., 2020) was used as a matrix-matched reference. Typical precision on a single $\delta^{34}\text{S}$ and $\delta^{18}\text{O}$ values, after propagating the within run and external uncertainties from the standard measurements was $\pm 0.2\text{‰}$ (1σ) and 0.23‰ (1σ), respectively. All results are reported with respect to the V-CDT (Ding et al., 2001) and V-SMOW (Coplen, 1994) for oxygen.

Carbonate concretions collected from the upper red sandstone and the bitumen-bearing sandstone were analyzed for stable carbon and oxygen isotope values at the NordSIMS facility at the Museum of Natural History, Stockholm, Sweden. The calcite intra-crystal SIMS-analysis were performed on the same Cameca IMS1280 described above. Settings follow those described for S isotopes, with some differences: O was measured on two F cups (FC) at mass resolution 2,500, C used a FC/Electron Multiplier combination with mass resolution 2,500 on the ^{12}C peak and 4,000 on the ^{13}C peak to resolve it from $^{12}\text{C}^1\text{H}$. Calcite results are reported as per mil (‰) $\delta^{13}\text{C}$ based on the Pee Dee Belemnite (V-PDB) reference value. Analyses were carried out running blocks of six unknowns bracketed by two standards. Analytical transects of up to nine spots were made from core to rim in the crystals. Up to five crystals were analyzed from each sample. Isotope data from calcite were normalized using calcite reference material S0161 from a granulite facies marble in the Adirondack Mountains, kindly provided by R. A. Stern (University of Alberta). The values used for instrumental mass fractionation correction were determined by conventional stable isotope mass spectrometry at Stockholm University on 10 separate pieces, yielding $\delta^{13}\text{C} = 0.22\text{‰} \pm 0.35\text{‰}$ V-PDB (1 SD) and $\delta^{18}\text{O} = -5.62\text{‰} \pm 0.22\text{‰}$ V-PDB (1 SD). Precision was $\delta^{18}\text{O}$: $\pm 0.2\text{‰}$ – 0.3‰ and $\delta^{13}\text{C}$: $\pm 0.4\text{‰}$ – 0.5‰ .

3. Results

3.1. Mineralogy and Textures

We divided the sandstone samples into four facies according to outcrop color: red, pink, yellow, and gray (Figure 1b). The gray facies is in the center of the sequence. Above the gray are the upper yellow, upper pink and red facies. Below the gray, stepping downward, are the lower yellow, pink, and red facies, mirroring the upper sequence (Figures 1 and 2). On average, the sandstone samples are medium-grained moderately sorted with ripple and cross-bed lamination, and grains are sub-angular to sub-rounded. We observe differences in texture, porosity, modal mineralogy, and geochemistry between the different colored facies. Each facies exhibit different iron-oxide and clay concentrations, in addition to variations in grain-coatings and pore-fill distributions and composition (Table 1 and 2, Figure 3).

Our point counting analysis shows a mineralogical composition of framework grains in the red facies of 90% quartz, 8.8% K-feldspar, and 1.6% plagioclase (Figure 3). Cement and pore-filling minerals consist of 38% iron-oxide grain coatings, 25% clay (mostly kaolinite), 17% iron-oxide cement, 15% calcite, and 5% silica. The thin coatings of finely dispersed iron-oxide grain coatings we observe occur with minor amounts of illite and surround nearly all detrital quartz and feldspar grains (Figures 4a and 4b). These coatings are responsible for the characteristic red color of the sandstone. We classified iron-oxide as “cement” when it was dominantly

Table 2
Average Unnormalized Concentration of Major Elements for the Colored Facies in the Slick Rock Member of the Entrada Sandstone

Facies	SiO ₂	TiO ₂	Al ₂ O ₃	Fe ₂ O ₃	MnO	MgO	CaO	Na ₂ O	K ₂ O	P ₂ O ₅	LOI %	Total
Red	86.28	0.11	3.60	0.66	0.06	0.24	3.26	0.00	1.80	0.03	3.48	99.51
Upper pink	74.07	0.09	3.02	0.73	0.36	2.81	7.16	0.00	1.57	0.02	9.51	99.36
Upper yellow	86.75	0.16	4.41	0.58	0.04	0.38	2.08	0.01	2.24	0.04	2.86	99.55
Gray	87.21	0.06	2.51	0.20	0.03	0.16	1.93	0.01	1.47	0.02	5.87	99.47
Lower yellow	88.49	0.12	4.13	0.54	0.03	0.25	1.48	0.01	2.15	0.03	2.23	99.45
Lower pink	91.08	0.07	2.90	0.37	0.07	0.13	1.42	0.00	1.60	0.02	1.83	99.48
Concretion	74.36	0.11	3.16	15.86	0.36	0.24	0.67	0.01	1.63	0.03	4.46	100.89

pore-filling, versus grain-coating, however, this iron-oxide is typically less than 50 μm in width and does not fully encase grains. The calcite cement is fine-grained, mottled, and evenly dispersed. Most K-feldspars show little to no alteration; however, we observe rare ghost feldspar grains that are filled with coarse-grained, platy, booklet-like clay particles.

The mineralogical composition of framework grains in the upper pink facies is 90% quartz, 8.0% K-feldspar, 1.6% plagioclase, and <1% accessory minerals. The cement and pore-filling minerals consist of 60% calcite,

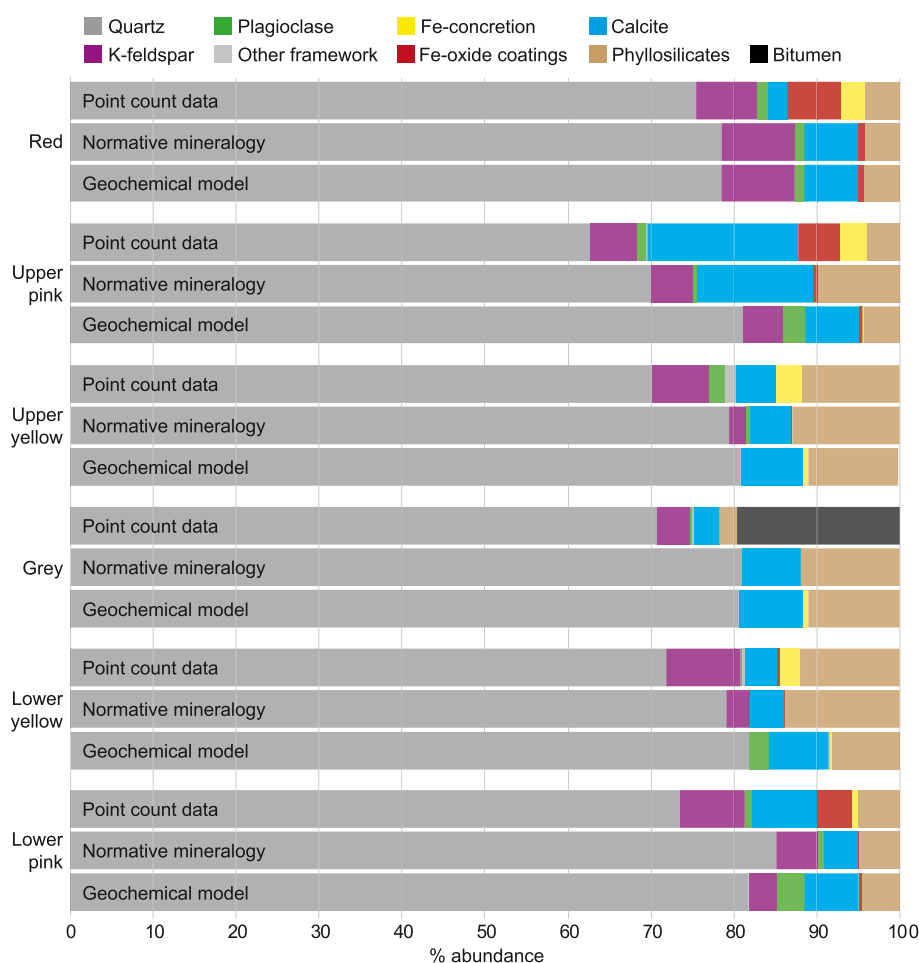


Figure 3. Average mineralogic composition of each facies from point count data, normative mineralogy calculated from the average major element data for each facies, and geochemical model results (see Section 4.5).

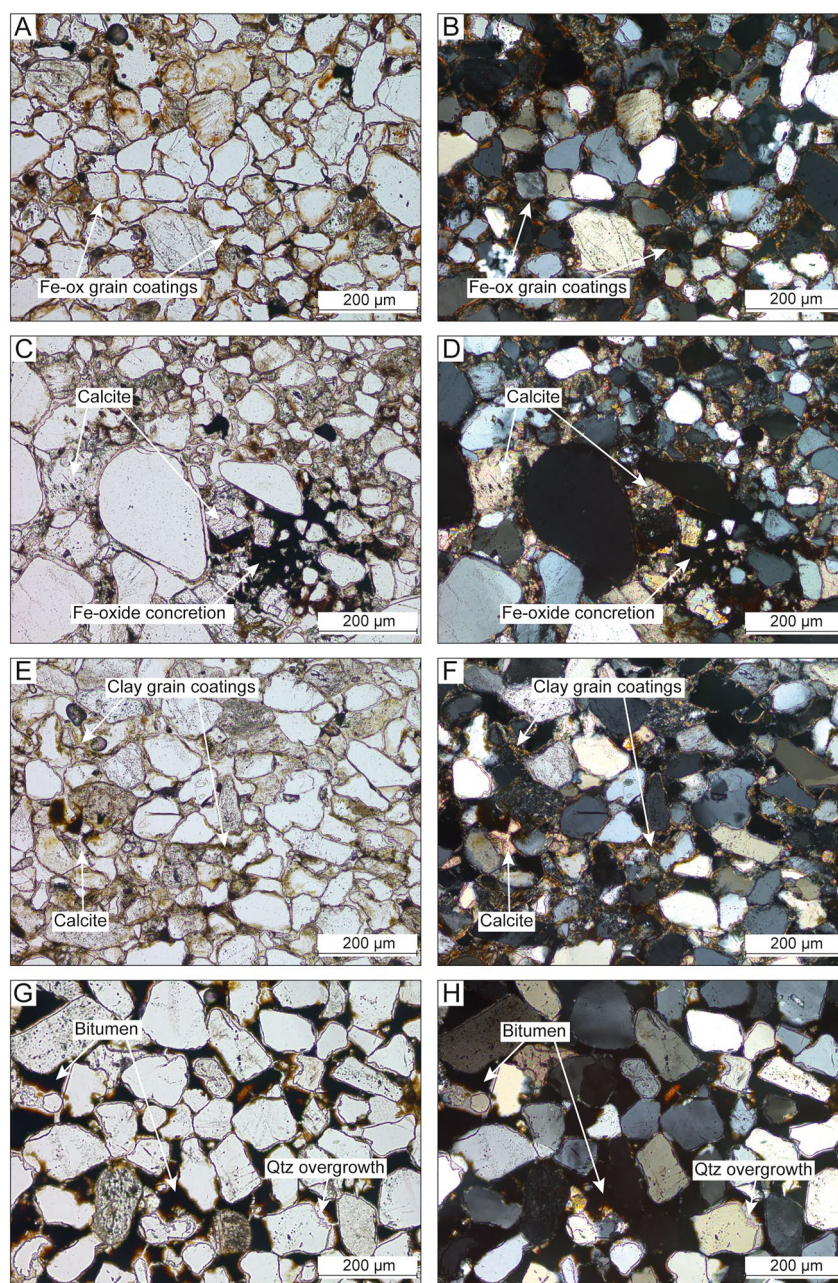


Figure 4. Representative thin section photomicrographs of the red (a, b), pink (c, d), yellow (e, f), and gray (g, h) sandstone facies. Photomicrographs on the left are under plane polarized light, those on the right are under cross polarized light.

17% iron-oxide grain coatings, 13% pore-filling clay, and 10% iron-oxide concretionary cement. The lower pink facies consist of 89.5% quartz, 9.5% K-feldspar, 1.1% plagioclase as framework grains. Calcite (44%), clay (29%), iron-oxide grain coatings (24%), and iron-oxide concretionary cement (3.8%) make up the cement and pore-fill. In contrast to the red facies, the iron-oxide and calcite cement, often closely associated, occur as larger, unevenly dispersed concretionary zones in both the upper and lower facies (Figures 2, 4c and 4d).

The upper yellow facies, according to our point counting, contains 88% quartz, 8.6% K-feldspar, 2.2% plagioclase, and <2% accessory minerals. The cement and pore fill consists of 60% fine-grained clay, 24% calcite, 16% iron-oxide concretion, and 1.1% quartz overgrowths (Figures 4e and 4f). The lower yellow facies has a very similar composition, consisting of 88% quartz, 11% K-feldspar, and <1% plagioclase and other accessory minerals. Cement and pore fill consists of 64% clay, 20% calcite, 13% iron-oxide concretions, 2.4% preserved

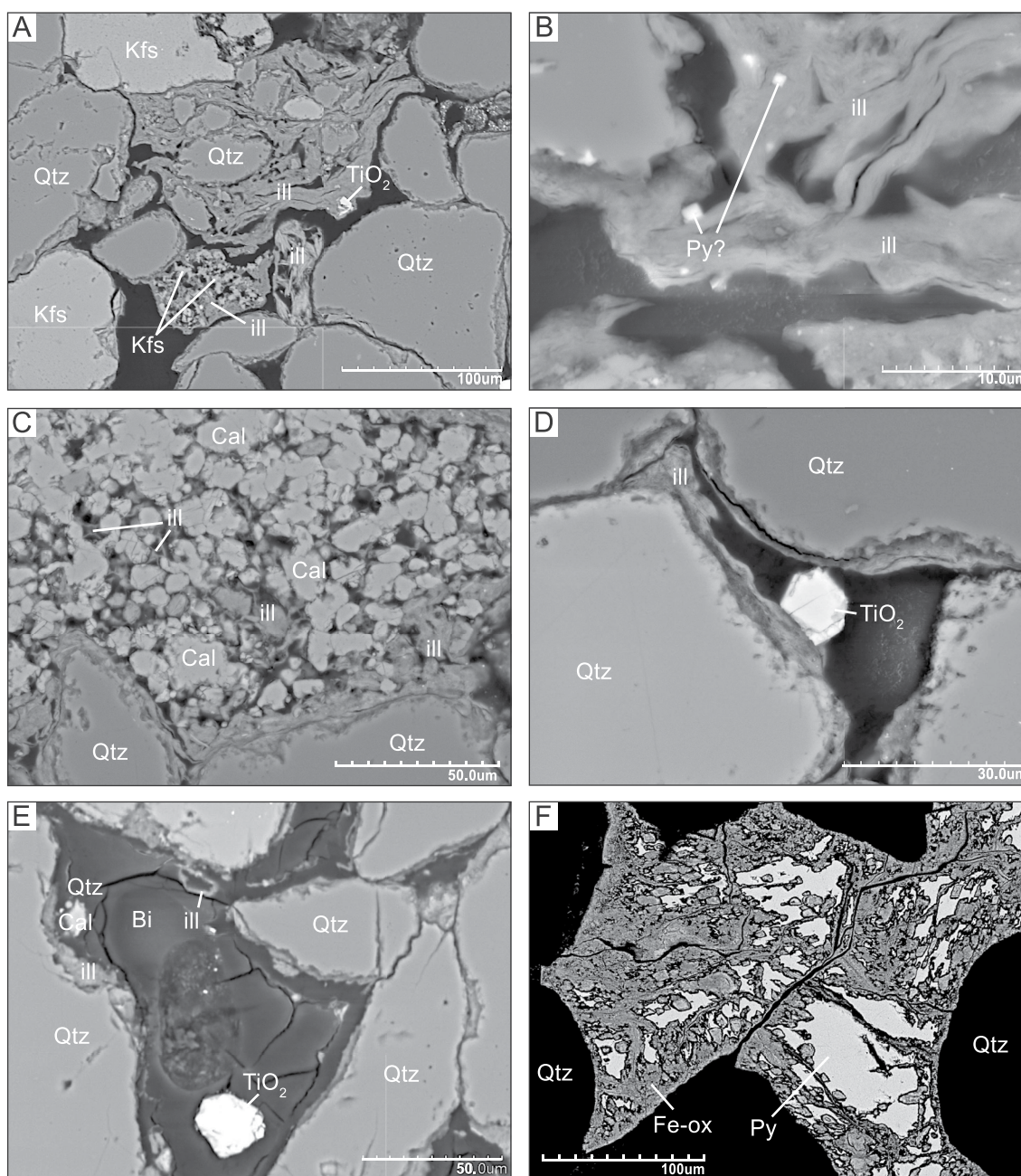


Figure 5. Back-scattered electron (BSE) images of key observations. (a) Quartz grains, intact and dissolved K-feldspar (Ksp), and coarse to fine-grained illite particles with TiO_2 in the yellow facies; (b) fine-grained “hairy” illite with small pyrite cubes (Py) in the yellow facies; (c) calcite (Cal) and illite pore-fillings in the yellow facies; (d) illite grain coatings with euhedral TiO_2 in the yellow facies; (e) pore-filling bitumen (Bi) with illite and euhedral TiO_2 in the gray facies; and (f) pyrite concretion in the gray facies that has been partially oxidized to iron-oxide (Fe-ox).

iron-oxide grain coatings, and 1.2% quartz overgrowths. The K-feldspar we observed was extensively altered, etched, and often exhibited intragranular pore spaces (Figure 5a). We observe very few hematite grain-coatings but abundant fine-grained “hairy” illite as grain coatings, pore linings, and intragranular relict K-feldspar pore fillings (Figures 5a and 5b). We also observe authigenic TiO_2 and calcite in the pore spaces, often closely associated with the hairy illite (Figures 5c and 5d), as well as very small cubes of (post-pyrite) iron-oxide (Figure 5b). Quartz overgrowths are ubiquitous (Figure 5a).

The gray facies comprise 94% quartz, 5.3% K-feldspar, and <1% plagioclase and other accessory minerals as framework grains. Cement and pore-filling minerals consist of bitumen (79%), calcite (13%), and clay (8.9%).

Bitumen fills nearly all pore-spaces, but we also observe irregular patches of coarse calcite cement (Figures 4g and 4h). Bitumen composes 20% of the gray facies, allowing us to estimate a porosity of approximately 20%. We see fine-grained illite as intragranular pore fillings, linings, and occasionally intergrown with bitumen, as well as euhedral authigenic TiO_2 and calcite within the bitumen (Figure 5e). The illite we observe in the gray and yellow facies has a distinct, fine-grained, “hairy” appearance in contrast to the coarse, platy clay minerals in the red facies. There are no iron-oxide grain coatings, but we observe spherical iron-oxide concretions in outcrop, approximately 5 mm to 2 cm in diameter, that are dispersed throughout the gray facies and have cores of remnant pyrite (Figures 2 and 5f). In one region of the exposure, we also observed blue azurite spherules in the gray facies, as documented by Chan et al. (2000). The azurite and iron-oxide concretions were not observed in the thin section.

3.2. Whole Rock Geochemistry

We observe significant differences in most major, minor, and trace elements between the red, pink, yellow, and gray facies, and substantial enrichment of major (e.g., Fe_2O_3 and MnO) and trace (Zn, Pb, Cu, U, and V) metals in concretions (Table 2, Figure 6). The plots in Figure 6 show element concentrations that have been normalized on a volatile (loss-on-ignition)-free basis. We observe average SiO_2 , Al_2O_3 , K_2O , and CaO concentrations of 90, 3.8, 1.9, and 3.4 weight %, respectively, in the red facies (Figures 6a–6c). Major metal concentrations are 0.68, 0.25, and 0.06 weight % for Fe_2O_3 , MgO, and MnO. Trace metals such as Zn, Pb, V, U, and Cu have concentrations of 10, 7.5, 16, 0.51, and 8.9 ppm, respectively (Figures 6d and 6f).

The upper pink facies has average SiO_2 , Al_2O_3 , and K_2O concentrations of 83, 3.4, and 1.7 weight %, respectively. This facies also has the highest CaO concentration (7.9 weight %) of all sampled sandstones. Major metal concentrations are 0.82, 3.1, and 0.41 weight % for Fe_2O_3 , MgO, and MnO, with MgO concentrations being the highest of all sampled sandstones. Trace metals Zn and V have concentrations of 38 and 31 ppm, higher than the red facies. Trace metals such as Pb and U have concentrations of 6.9 and 0.44 ppm, slightly lower than the red facies, while other elements such as Cu (8.2 ppm) and the majority of REE have similar concentrations to the red facies. The lower pink facies has higher SiO_2 (93%), lower Al_2O_3 (2.9%), and similar K_2O (1.7%) than the upper pink facies. Concentrations of major metals such as Fe_2O_3 (0.38%), MgO (0.13%) and MnO (0.07%) in the lower pink facies are lower than the upper pink and red facies (except MnO). Trace metals Zn and V have lower concentrations (11 and 18 ppm, respectively) than the upper pink facies, but are like that of the red facies. Uranium (0.38 ppm), Pb (5.9 ppm), Cu (7.8 ppm) and REE all have slightly lower concentrations than both the upper pink and red facies.

The upper yellow facies has average SiO_2 , Al_2O_3 , and K_2O concentrations of 90, 4.6, and 2.3 weight %, respectively, all higher than pink and red facies. CaO concentrations (2.2%) and major metal concentrations of 0.60, 0.39, and 0.04 weight % for Fe_2O_3 , MgO, and MnO, respectively, are low relative to the pink and red facies. Trace metals Zn and V have concentrations of 16 and 19 ppm. Trace metals such as Pb (7.6 ppm), U (0.73 ppm), and Cu (12 ppm) and most REE have concentrations that are higher than the aforementioned facies. The lower yellow facies has similar average SiO_2 (91%), Al_2O_3 (4.3%), K_2O (2.2%), Fe_2O_3 (0.55%), and MnO (0.03%) concentrations to the upper yellow unit. In contrast, CaO (1.5%) and MgO (0.26%) concentrations are slightly lower. Trace metals Zn and V have concentrations of 12 and 22 ppm, respectively. Lead and U have concentrations of 7.6 and 0.76 ppm, like the upper facies, whereas Cu concentrations (13%) are higher. All REE concentrations are lower than that of the upper yellow facies, but like the red facies. TiO_2 and all other HFSE concentrations in the upper and lower yellow facies are higher than all other colored facies (Figure 6e).

The gray facies contains relatively higher SiO_2 concentrations (93%), but has the lowest Al_2O_3 (2.7%) and K_2O (1.6%) concentrations of all facies. The CaO concentration is 2.1%. In contrast to all the facies mentioned above, the Fe_2O_3 concentration is also the lowest at 0.21%, however, MgO (0.17%) and MnO (0.04%) concentrations are similar to the lower pink or yellow facies, respectively. Zinc and Pb have the lowest concentrations in the gray facies at 6.3 and 4.3 ppm, respectively. The gray facies also exhibits the lowest concentrations in all REE and HFSE. Vanadium concentrations (23 ppm) are similar to the other altered facies (e.g., yellow and lower pink), but higher than the red facies. In comparison to all other facies, Cu and U concentrations are significantly higher at 60 and 1.2 ppm.

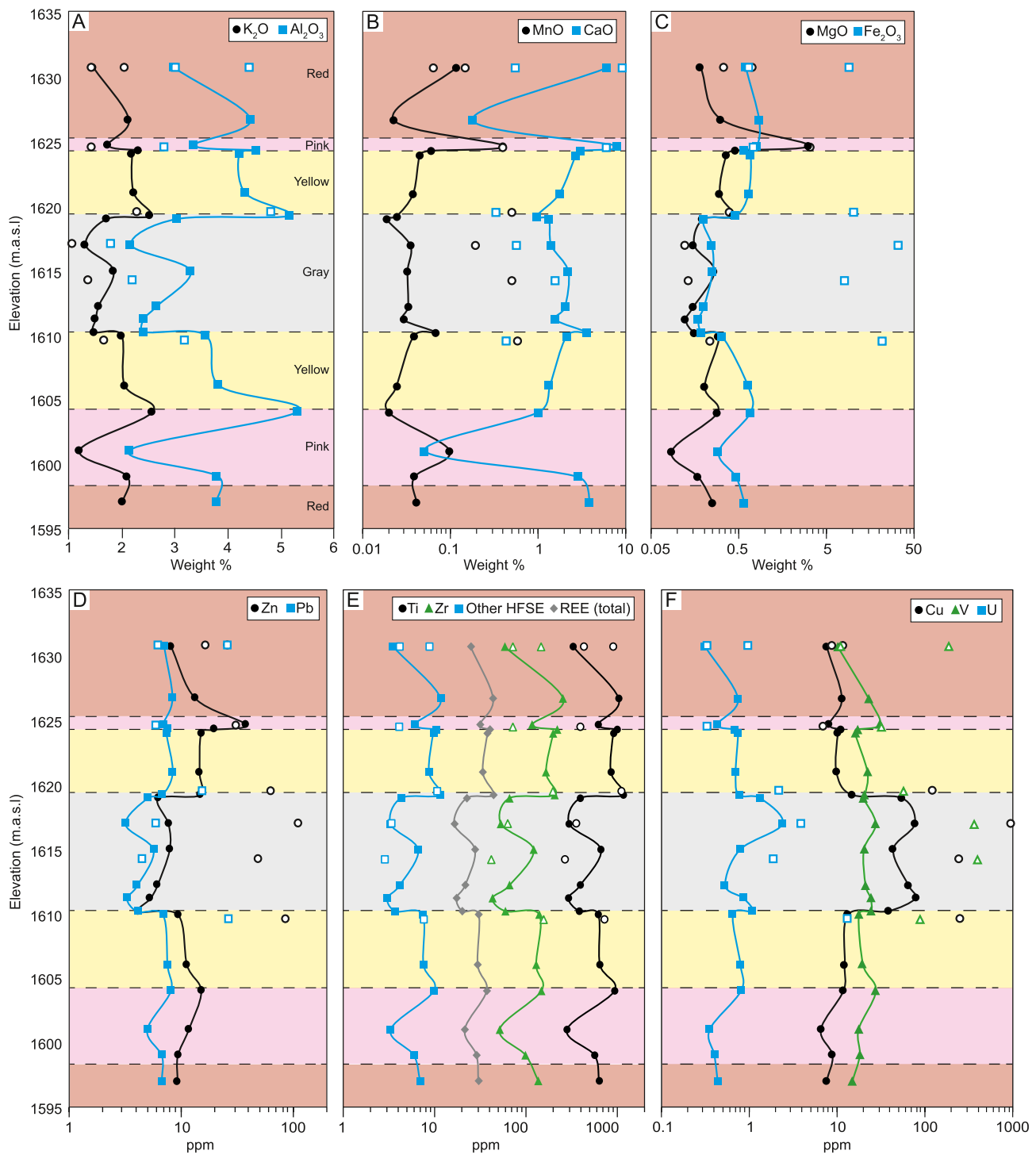


Figure 6. Major (a–c), minor, and trace (d–f) element data for sandstone facies and concretions sampled across the transect. Data for sandstone samples are solid symbols, open symbols for concretions.

In the sampled iron-oxide concretions, we see that the SiO_2 concentrations range from 66% to 84%, but on average have lower concentrations (78%) than the sandstone samples. The concentrations of Al_2O_3 (3.3%) and K_2O (1.7%) are comparable to those of the pink facies, but CaO concentrations (0.71%) are lowest in the iron-oxide concretions. Evidently, Fe_2O_3 concentrations are much higher in the concretions and range from 8.2% to 34%. The average MnO (0.38%) and MgO (0.25%) concentrations are also relatively high. The concretions have significantly

Table 3
Calcite Carbon and Oxygen Stable Isotopic Compositions, and Calculated Oxygen Isotope Values of the Parent Fluid

Sample ID	Facies	$\delta^{13}\text{C}$	$\pm \text{‰}$	$\delta^{18}\text{O}$	$\pm \text{‰}$	20°C	50°C	90°C
						$\delta^{18}\text{O}\text{-H}_2\text{O (‰) of calculated waters}$		
18PRPB08A	Red	−3.53	0.48	−12.79	0.28	−11.45	−5.79	0.34
18PRPB08A	Red	−3.84	0.46	−12.65	0.24	−11.30	−5.64	0.49
18PRPB08A	Red	−3.45	0.42	−17.09	0.27	−15.75	−10.12	−4.02
18PRPB08A	Red	−4.39	0.44	−13.88	0.26	−12.54	−6.88	−0.76
18PRPB08A	Red	−4.28	0.48	−13.09	0.25	−11.75	−6.09	0.03
18PRPB08A	Red	−1.77	0.48	−12.54	0.24	−11.20	−5.54	0.59
18PRPB19	Gray	−5.39	0.46	−15.58	0.28	−14.24	−8.60	−2.48
18PRPB19	Gray	−7.15	0.49	−12.80	0.27	−11.45	−5.79	0.33
18PRPB19	Gray	−5.24	0.48	−15.59	0.24	−14.26	−8.61	−2.50
18PRPB19	Gray	−6.65	0.47	−20.37	0.26	−19.04	−13.42	−7.34
18PRPB19	Gray	−6.00	0.51	−12.92	0.27	−11.58	−5.92	0.21
18PRPB19	Gray	−6.25	0.45	−13.69	0.25	−12.35	−6.69	−0.57
18PRPB19	Gray	−6.21	0.44	−12.88	0.28	−11.54	−5.88	0.25
18PRPB19	Gray	−5.79	0.45	−12.79	0.33	−11.44	−5.78	0.35
18PRPB19	Gray	−6.25	0.45	−12.05	0.26	−10.71	−5.04	1.09
18PRPB19	Gray	−9.68	0.41	−13.27	0.27	−11.93	−6.27	−0.14
18PRPB19	Gray			−11.93	0.25	−10.58	−4.92	1.21
18PRPB19	Gray	−8.20	0.44	−19.06	0.25	−17.72	−12.10	−6.01
18PRPB19	Gray	−5.66	0.50	−13.47	0.27	−12.13	−6.47	−0.35

higher concentrations of most trace metals such as Zn (68 ppm), Ni (18 ppm), Pb (16 ppm), V (219 ppm), U (4.5 ppm), and Cu (327 ppm). REE concentrations are comparable to the yellow facies, but HFSE concentrations fall between the gray and yellow facies.

Overall, the most notable differences that we observed between the facies are (a) comparatively high Al_2O_3 and K_2O concentrations in both yellow facies; (b) enrichment of Cu and U in the gray facies; (c) V enrichment in all “altered” facies compared to the red facies; (d) reduction in Fe_2O_3 concentration by more than a factor of three, from an average of 0.68% in the red, to 0.21% in the gray facies; (e) lowest concentrations of all REE, HFSE, and trace metals Zn and Pb, in the gray facies; and (f) all trace metals including Zn, Pb, Cu, U, and V are enriched in the iron-oxide concretions. The enrichment of Al_2O_3 and K_2O in the yellow facies coincides with greater modal proportions of illite. Specifically, we observe the highest Al_2O_3 and K_2O concentrations at the boundary between both the upper and lower pink and yellow facies. We observe concentrations of up to 985 ppm of Cu and 400 ppm of V in iron-oxide concretions that contain cores of pyrite.

3.3. Stable Isotopes

3.3.1. Calcite

Calcite cement from the gray facies has $\delta^{13}\text{C}$ values (relative to VPDB) that range from $-5.2\text{‰} \pm 0.5\text{‰}$ to $-9.7\text{‰} \pm 0.4\text{‰}$, with an average of $-6.5\text{‰} \pm 1.3\text{‰}$ (Table 3; Figure 7a). Calcite cement from the red facies has $\delta^{13}\text{C}$ values that are less negative and range between $-1.8\text{‰} \pm 0.5\text{‰}$ and $-4.4\text{‰} \pm 0.4\text{‰}$, with an average of $-3.5\text{‰} \pm 1.0\text{‰}$ (Figure 7a). The $\delta^{18}\text{O}$ values, however, overlap for the two calcite cements. The average $\delta^{18}\text{O}$ values (VPDB) for cement in the gray and red facies are $-14.3\text{‰} \pm 2.6\text{‰}$ and $-13.7\text{‰} \pm 1.7\text{‰}$, respectively (Figure 7a).

Figures 7b and 7c show $\delta^{18}\text{O}$ and $\delta^{13}\text{C}$ data from our study alongside compiled, previously published stable isotope data of calcite veins, cement, concretions, and whole rock samples from the Paradox Basin. Cement from

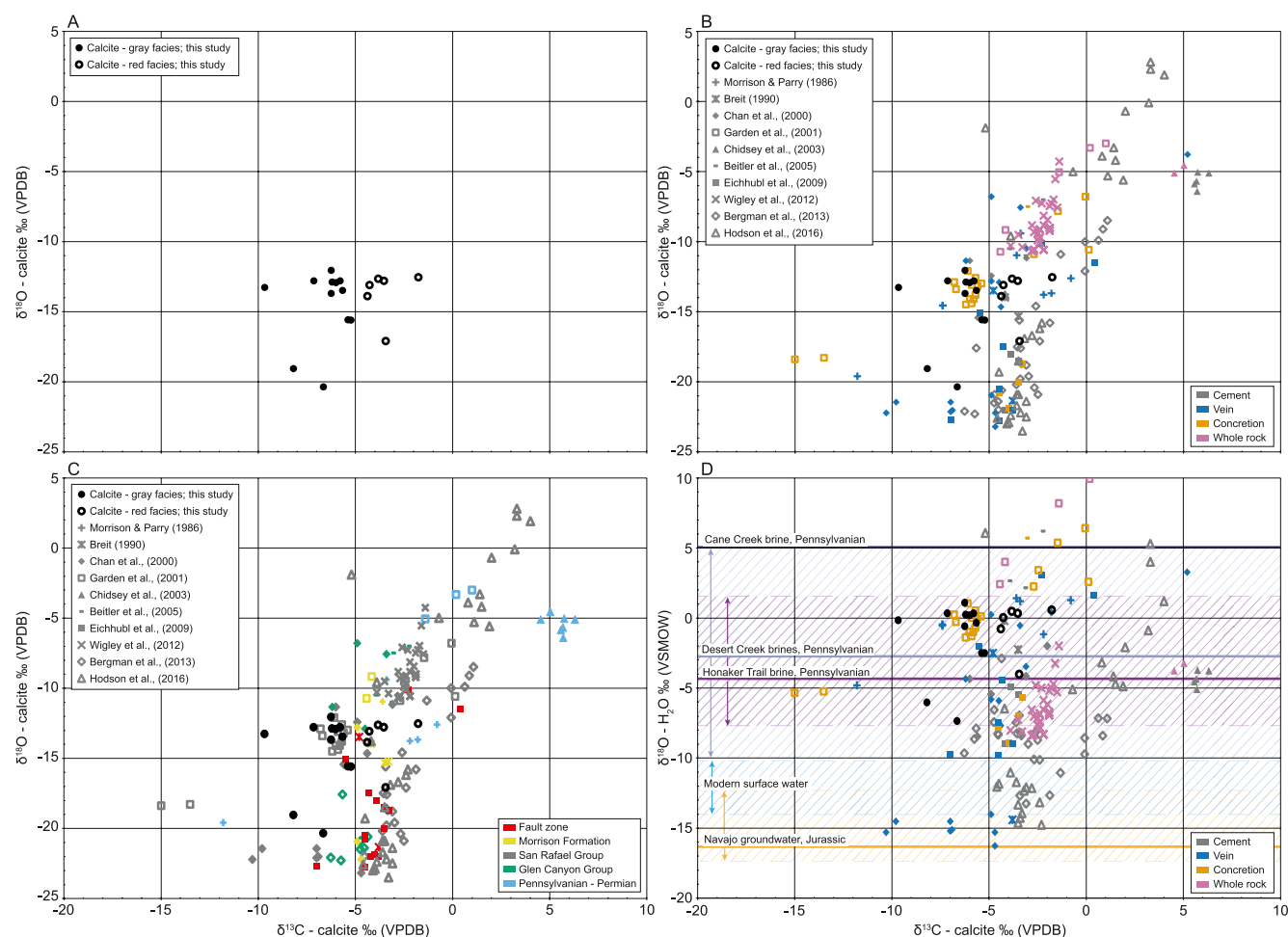


Figure 7. (a) Carbonate isotope data from calcite from the unbleached (open circles) and bleached (closed circles) from our study; (b) our data plotted with previously published stable isotope data of calcite veins, cement, concretions, and whole rock collected from the Paradox Basin; (c) our data plotted with previously published stable isotope data sorted by formation; and (d) calculated $\delta^{18}\text{O}-\text{H}_2\text{O}$ compositions of compiled cement, vein, concretion, and whole rock data using temperature estimates plotted with the $\delta^{18}\text{O}-\text{H}_2\text{O}$ ranges of modern water from the Paradox Basin (J.-H. Kim et al., 2022).

the red facies has similar carbon isotopic values to calcite cements sampled from the Moab Member of the Curtis Formation near the Moab Fault (Bergman et al., 2013; Hodson et al., 2016). Bergman et al. (2013) suggested a dominantly meteoric source for fluids from which these cements precipitated. The carbon isotopic compositions of the red facies cement is also similar to those of whole rock bleached Entrada Sandstone from Green River (Wigley et al., 2012). Wigley et al. (2012) suggested organically derived bicarbonate was not a major source of carbon in secondary carbonates at Green River, but the heavier oxygen isotope values suggests the parent fluid contained basinal brines. Calcite cement sampled from the gray facies have isotopic compositions similar to calcite concretions in the Entrada Sandstone from the Moab Anticline (Garden et al., 2001) and calcite veins associated with bitumen near the Moab Fault (Chan et al., 2000), where Garden et al. (2001) interpreted the bleached sandstone as a paleo-hydrocarbon migration fairway.

In summary, cement collected from the gray facies has similar carbon isotopic compositions to some veins and concretions that are hosted in bleached sections of the Entrada Sandstone or Curtis formation and associated with bitumen (Figures 7b and 7c). Cement collected from the red facies has similar carbon isotopic compositions to veins and cements (Figure 7b) collected from the Entrada Sandstone or Curtis formation close to fault zones (Figure 7c). The oxygen isotopic compositions we measured for cement from both the red and gray facies is like other concretions collected from the Slick Rock member of the Entrada Sandstone (Figure 7b; Garden et al., 2001), however the entire compiled data set show a large range of values from -24‰ to $+3\text{‰}$.

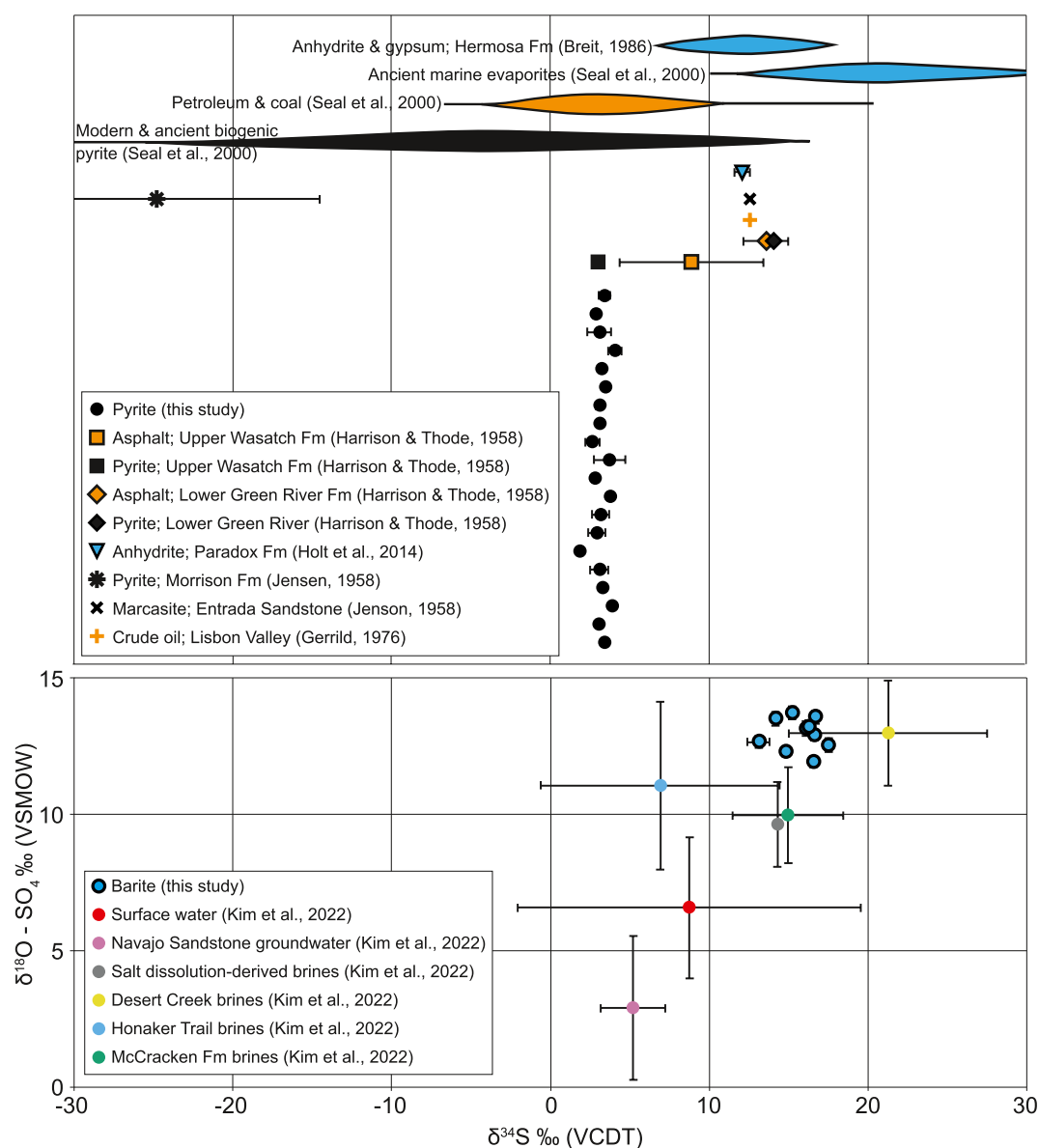


Figure 8. Upper panel: Sulfur isotopes for pyrite collected from the gray facies compared to data from the Paradox Basin. Lower panel: S and O isotopes of barite collected from the red facies compared to S and O isotopes of present-day brines and groundwater from the Paradox Basin.

3.3.2. Barite and Pyrite

The sulfur ($\delta^{34}\text{S}$) and oxygen ($\delta^{18}\text{O}$) isotopic composition of barite collected from the red sandstone are $+15.4\text{‰} \pm 1.4\text{‰}$ and $+12.9\text{‰} \pm 0.6\text{‰}$, respectively (Figure 8). Residual pyrite collected from the top of the bitumen-bearing gray sandstone has a sulfur isotope composition of $+3.3\text{‰} \pm 0.5\text{‰}$ ($n = 57$; Figure 8), displaying very little variation within and between grains. The sulfur isotope composition of the barite is similar to that of gypsum in nearby interbedded evaporites of the Hermosa Formation and barite from the Morrison Formation (Figure 8; Breit, 1986; Breit & Meunier, 1990). The barite also has sulfur isotope compositions similar to brines derived from salt dissolution or the McCracken Formation, and oxygen isotope compositions similar to Desert Creek brines from the Paradox Formation (J.-H. Kim et al., 2022). The pyrite we sampled is more enriched in ^{34}S in comparison to sulfides from sandstone-type uranium or copper deposits on the Colorado Plateau, where sulfides hosted in the Morrison and Entrada formations have $\delta^{34}\text{S}$ values ranging from approximately -35‰ to -14‰ (Jensen, 1958). On the other hand, sulfur isotope compositions of pyrite from hydrocarbon source rocks

in the Uinta Basin range from +3‰ (Upper Wasatch Formation) to +29‰ (Upper Green River) (Harrison & Thode, 1958). Crude oil from the Lisbon oil field, sourced from the Leadville Limestone, has a $\delta^{34}\text{S}$ value of 12.6‰ (Gerrild, 1976).

4. Discussion

Beitler et al. (2003) suggest that the color variations in the Jurassic Navajo Sandstone are evidence of a hydrocarbon supergiant reservoir, where bleaching was interpreted to be accomplished by secondary migration of hydrocarbons. Similarly, Gorenc and Chan (2015) assume that the bleaching observed in the White Rim Sandstone in the nearby Elaterite Basin was also due to hydrocarbon migration. Based on the presence of bitumen saturated pore spaces, mineralogic changes, and major and trace element variations we hypothesize that the Slick Rock member of the Entrada Sandstone at our study site was a paleo-hydrocarbon migration fairway, similar to that from the Moab Anticline (Garden et al., 2001).

However, some questions remain, which we attempt to address in the following discussion: (a) when did hydrocarbon migration occur; (b) what was the source of the hydrocarbons and associated aqueous fluids; (c) did hydrocarbon flow mobilize significant amounts of iron and other elements out of the affected units; (d) if so, how far were these mobilized elements transported; (e) how did the hydrocarbons migrate into the Slick Rock member of the Entrada Sandstone; and (e) why were the hydrocarbons confined to a specific horizon?

4.1. Timing of Fluid Migration

Petrographic observations of the yellow sandstone show substantial authigenic fine-grained “hairy” illite as grain coatings, pore linings, and pore fillings in dissolved, relict K-feldspar. The intergrowth of illite and bitumen in the gray sandstone in our study area suggests authigenic illite precipitation was contemporaneous with hydrocarbon charge (Wilkinson et al., 2006). Lee et al. (1989) noted that K-Ar age determinations on the finest grained, last-formed illite constrains the timing of hydrocarbon charge, as illite is often the last mineral to form prior to hydrocarbon charge into a reservoir. Bailey et al. (2022) showed that interstitial authigenic clay from the yellow facies in our study area formed 41.1 ± 2.5 Ma. This age is younger than the proposed timing of oil migration into the Moab Anticline at 49–63 Ma, implied from paleomagnetic results discussed in Garden et al. (2001). According to Gorenc and Chan (2015), hydrocarbons entered the White Rim Sandstone between 35 and 40 Ma, coincident with maximum burial depths inferred by Huntoon et al. (1999). The timing of clay formation in our study site is coeval with the timing of maximum burial and a late stage of hydrocarbon generation near Moab proposed by Nuccio and Condon (1996).

4.2. Bleaching Agents

Reduced fluids such as liquid hydrocarbons, CH_4 , and CO_2 have been proposed as bleaching agents responsible for producing the observed variations in sandstone colors across the Colorado Plateau (e.g., Beitler et al., 2005; Chan et al., 2000; Garden et al., 2001; Gorenc & Chan, 2015; Loope et al., 2010; Wigley et al., 2012; Xie et al., 2021). Eichhubl et al. (2009) suggested that reducing aqueous fluids that have been in contact with oil, rather than hydrocarbons directly, are more likely to be responsible for the bleaching due to the low solubility of hematite in oil. Other possible reducing fluids include organic acids, such as acetate, or hydrogen sulfide. Organic acids can be generated in situ from kerogen or from emplaced petroleum in reservoir rocks (Barth & Bjørlykke, 1993) during aerobic or anaerobic microbial oxidation (Watson et al., 2002). Enhanced generation of organic acids has also been shown to occur during kerogen oxidation by oxygen generated from the reduction of ferric oxide (Lewan & Fisher, 1994), so it is possible that both oil and organic acids can be responsible for bleaching simultaneously. Organic acids can readily dissociate to CO_2 and CH_4 , and several studies have suggested that CO_2 and CH_4 are the main drivers of sandstone bleaching in areas of the Colorado Plateau where solid bitumen is not observed (Loope & Kettler, 2015; Wigley et al., 2012, 2013). Xie et al. (2021) observed similar diagenetic changes as those documented in our study in deep red-beds in the Ordos Basin, China, including K-feldspar dissolution, illite and calcite precipitation, and Ti mobilization. These were interpreted as resulting from CH_4 migration.

Although a range of reducing fluids may be responsible, many studies invoke migration of hydrocarbons as the bleaching agent for Jurassic sandstones on the Colorado Plateau. For example, Beitler et al. (2003) suggest that

the large-scale bleaching patterns observed in the Navajo Sandstone reflect an exhumed “supergiant” hydrocarbon reservoir. Only a few of these studies document direct evidence of hydrocarbons such as hydrocarbon-bearing fluid inclusions (e.g., Garden et al., 2001; Gorenc & Chan, 2015) or remnant interstitial bitumen. Otherwise only indirect observations such as reduction patterns are used to speculate the type of fluid responsible for the observed bleaching, for example, “ponding” of the bleached sandstones at crests of anticlines potentially indicate that the fluids were buoyant and immiscible (Garden et al., 2001). We suggest that interstitial bitumen in some previous studies has been misidentified and is in fact ~10 to 200 μm -sized Fe-oxide concretions. Bitumen is brittle and often displays shrinkage cracks or shrinkage away from grains when observed in thin section due to loss of volatiles (Shalaby et al., 2012; Womer, 1986). Other characteristics typical of solid bitumen that can help distinguish from Fe-oxide concretions include smooth, curved meniscate margins, void- and fracture-filling habit, and sometimes internal flow structures (J. M. Wood et al., 2018). In our study area, the bitumen is pervasive and fills all pore spaces in the gray facies in contrast to the Fe-oxide concretions that are unevenly distributed. Fe-oxide concretions do not show convex meniscate margins nor the typical “cracks,” but instead have irregular margins. Small (50–200 μm) dark-colored Fe-oxide concretions in some bleached sandstones may be confused with bitumen in hand sample, and we suggest that energy dispersive x-ray spectroscopy (EDS) measurements provide a useful way to distinguish between bitumen and Fe-oxide concretions.

Bitumen saturated pore-spaces in the gray facies in our study area clearly implicates oil migration through this section of the Entrada Sandstone was responsible for bleaching, and the other mineralogic and geochemical differences we observe across the different colored facies. The presence of pyrite in the core of iron-oxide concretions in the gray facies, as well as sulfur concentrations from 3% to up to 16% in the preserved bitumen (EDS measurements), indicates that the hydrocarbons responsible for bleaching at Rainbow Rocks contained sulfur. Oil extracted from oil-impregnated Jurassic sandstones from Ten Mile Wash, located just 7 km north of the study area, contains up to 4.2% total sulfur (R. E. Wood & Ritzma, 1972). In fact, the extracted oil was likely collected from the same bitumen-saturated sandstone layer from our study. R. E. Wood and Ritzma (1972) suggest that the oil migrated up faults into the Jurassic sandstones from Permian or older formations. The nearby Salt Wash oil field produces oil from the Leadville limestone, where the produced hydrocarbon liquids contain 0.13% S (Chidsey, 2009). Organic-rich black dolomitic shales from the Pennsylvanian Paradox Formation are the probable source rocks for the Salt Wash field (Chidsey, 2009). Experimental studies have shown that a small amount of H_2S with CO_2 mobilized more iron from red sandstone in comparison to CH_4 and CO_2 , or CO_2 alone (Purser et al., 2014). Overall, the bitumen responsible for bleaching of our studied section was likely sourced from the Pennsylvanian Paradox Formation and possibly contained up to 4.2% total sulfur that enabled the mobilization of more iron and the formation of pyrite.

Coarse-grained calcite cement in the gray facies exhibits more negative $\delta^{13}\text{C}$ values compared to the fine grained, mottle calcite cement observed in the red facies. Many studies on bleached sandstones from the Colorado Plateau suggest secondary calcite formation is associated with reaction with hydrocarbons and/or CH_4 and CO_2 (Garden et al., 2001; Wigley et al., 2012). Gorenc and Chan (2015) interpret the secondary calcite to be late-stage cement formed during exhumation and the influx of oxidizing meteoric fluids, whereas others suggest precipitation to be contemporaneous with bleaching (Garden et al., 2001; Wigley et al., 2012), or due to aerobic or anaerobic petroleum oxidation (Kirkland et al., 1995; Schumacher, 1996). Wigley et al. (2012) showed that the acidity of the system is buffered by the precipitation/dissolution of calcite due to the reactions fast kinetics. K-feldspar dissolution consumes acidity, which can initiate calcite precipitation. On the other hand, acetic acid or acidity generated from dissolved CO_2 can dissolve calcite cements.

We observe a systematic shift of carbon isotope compositions from approximately -3.5‰ for the red sandstone-hosted calcite cement to -6.5‰ for calcite in the gray facies. Several other studies from the Colorado Plateau also show a shift to more negative values in altered sandstones (Figure 7; Chan et al., 2000; Garden et al., 2001). If this shift was due to temperature-based fractionation, and both calcite populations were sourced from the same carbon pool, a temperature difference of $\sim 106^\circ\text{C}$ is required. The Entrada Sandstone was buried to a maximum temperature of $\sim 80^\circ\text{C}$ according to 1D burial models (Garden et al., 2001; Nuccio & Condon, 1996). Therefore, we suggest the shift is more consistent with a contribution of carbon from organic material in the gray-facies calcite. Schumacher (1996) states that calcite formed from oxidized petroleum should have carbon isotopic compositions from -10 to as low as -60‰ . Therefore, we suggest a hybrid source of groundwater and hydrocarbons is most likely reflected in these calcite isotopic compositions. If we assume the $\delta^{13}\text{C}$ compositions

of the calcite in the red facies represent the average groundwater value during the time of calcite precipitation, and use -27‰ for a hydrocarbon source, then 33% of the $\text{HCO}_3^-/\text{CO}_2$ that contributed to calcite precipitation was sourced from hydrocarbons and 66% from groundwater. Garden et al. (2001) suggested calcite concretions with $\delta^{13}\text{C}$ below -13‰ indicate extraformational, organically derived carbonate from liquid or gaseous hydrocarbon fluids.

To estimate the oxygen isotopic compositions of the parent paleofluid from which the calcite precipitated, paleofluid temperatures are needed due to the temperature dependence of oxygen equilibrium isotopic fractionation between water and calcite. Some of the compiled isotopic data from previous studies included temperature estimates from clumped isotope thermometry (Bergman et al., 2013; Hodson et al., 2016) or fluid inclusion homogenization temperatures (Breit & Meunier, 1990; Eichhubl et al., 2009; Morrison & Parry, 1986; Wigley et al., 2012). Otherwise, temperature ranges suggested by the authors (Beitler et al., 2005; Chan et al., 2000; Garden et al., 2001), or temperatures of maximum burial of Jurassic sandstones as suggested by Nuccio and Condon (1996), were used to calculate the temperature-dependent fractionation factors and the parent fluid oxygen isotopic compositions (S.-T. Kim & O'Neil, 1997). The calculated oxygen isotope values of the parent fluid compositions ($\delta^{18}\text{O}\text{-H}_2\text{O}$ in VSMOW) were plotted against $\delta^{13}\text{C}$ of calcite (Figure 7d). Ranges of $\delta^{18}\text{O}$ for the Cane Creek, Desert Creek, and Honaker Trail paleo-evaporated seawater derived brines from the Pennsylvanian Paradox Formation, fresh groundwater from the Jurassic Navajo sandstone, and modern surface water from J.-H. Kim et al. (2022) were plotted with the calcite data (Figure 7d). Most samples plot between the most $\delta^{18}\text{O}$ -enriched Cane Creek brine and fresh groundwater from the Navajo sandstone and likely formed from a mixed-source fluid. Although the temperature estimates based on burial curves will result in considerable uncertainty on the resulting parent isotopic compositions, the goal was to evaluate potential fluid sources for the calcite.

Using a temperature estimate of 80°C , based on the burial temperature for Jurassic formations at 41 Ma (Nuccio & Condon, 1996), our data from calcite of the Entrada Slickrock Member falls in the range of values represented by Pennsylvanian seawater derived brines from the Paradox Basin (-7‰ to $+2\text{‰}$; Table 3, Figure 7d). The black shales of the Pennsylvanian Honaker Trail and Paradox Formations are likely source rocks for the hydrocarbons and associated brines that migrated into the sandstone. Using a temperature estimate of 20°C , our data from the Entrada Slickrock Member would have similar $\delta^{18}\text{O}\text{-H}_2\text{O}$ to modern groundwater from the Navajo sandstone (-11‰ to -19‰ ; Table 3; Figure 7d).

4.3. Sandstone Bleaching and the Fate of Iron

Many previous studies denote yellow and white eolian sandstones of the Colorado Plateau as “bleached,” referring to the removal and dissolution of iron-oxide grain coatings by reaction with reduced aqueous fluids or hydrocarbons (e.g., Beitler et al., 2003, 2005; Chan et al., 2000; Loope et al., 2010). The red pigment of many well-studied sandstone deposits in Utah is formed by thin iron-oxide coatings on framework grains that are formed during early diagenesis under oxidizing conditions (Walker et al., 1981). Our results suggest that as little as 0.6% Fe_2O_3 is sufficient to create a strong red pigment in the red facies (e.g., Figure 4a), however it is likely that mineralogic form and intergranular distribution of the iron is more important than its concentration.

Most of the altered sandstone facies have lower Fe_2O_3 concentrations than the red facies (0.68%), however we do observe higher concentrations of Fe_2O_3 in the upper pink sandstone (0.82%). In contrast to the other samples, the iron in the upper pink facies is in the form of irregular patches of Fe (Mn)-cement, and the grain coatings we observe are very thin, if not missing, hence an overall pink pigment. The gray (0.21%), lower pink (0.38%), upper (0.60%) and lower (0.55%) yellow facies have lower concentrations of Fe_2O_3 . The yellow and gray facies have no iron-oxide grain coatings, but host yellowish, brown, to black iron-concretions. Beitler et al. (2005) suggested goethite, versus hematite, concretions provide yellowish to brownish outcrop colors. The range of sandstone colors we observe at Rainbow Rocks can be attributed to the different concentrations, and form (such as grain coatings, concretions, or cement), of Fe_2O_3 .

Although only very minor concentrations of iron-oxide are required to form a red pigment in the sandstones, white and yellow (“bleached”) sandstones can span laterally tens of kilometers throughout the Colorado Plateau, suggesting large-scale iron reduction and/or redistribution. Whether iron is (a) transported long distances (hundreds to thousands of meters) and reprecipitated in distal oxidized zones (e.g., Garcia et al., 2018), (b) reprecipitated in-situ as disseminated cement around pre-existing iron-oxide, siderite, or calcite concretions (Loope

et al., 2012; Yoshida et al., 2018), or (c) redistributed locally (at centimeter to meter scales) in concretions, is often not known, and may vary from site to site. Many studies suggest that the mobilized iron is re-deposited as iron-oxide or siderite concretions that are often found at the reaction front between red (oxidizing) and white (reducing) sandstones (Beitler et al., 2005; Chan et al., 2000; Gorenc & Chan, 2015; Loope & Kettler, 2015; Loope et al., 2010).

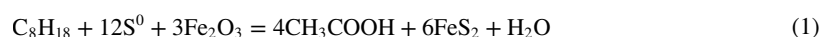
Although the lower Fe_2O_3 concentrations in the yellow and gray facies are consistent with the removal of iron from the section, it is possible that this iron precipitated and can be accounted for in the concretions. Therefore, to assess if iron has been transported long distances or redistributed and precipitated into concretions more locally at our study site, we can use the differences in iron concentrations across the facies to conduct a mass balance calculation. We assume that the sandstone colors and differences in iron concentrations are a result of reduced fluid flow, rather than initial compositional and mineralogical differences during deposition. We also assume that the entire section had an initial composition and Fe_2O_3 concentration equivalent to that of the red facies (0.68%). We used the thicknesses of each facies in the section, compared to the overall thickness (27 m), to calculate the proportion of Fe_2O_3 hosted in each facies. From this, we estimate that 34% of Fe_2O_3 in the originally red section has been removed due to flow of reduced fluids, not accounting for Fe_2O_3 hosted in concretions. For concretions with an average Fe_2O_3 concentration of 16.8% to balance the iron removed from the sandstone, their abundance throughout the bleached section would have to be approximately equal to a cumulative thickness of about 0.4 m, up to 1.5% of the overall thickness. The concretions we observe at the study site range from <1 to 15 cm in diameter, with a discontinuous and irregular spacing in the lateral direction. However, concretions are typically concentrated along specific horizons in the studied section, and have a maximum cumulative thickness of approximately 0.4 m. If we assume that this thickness of concretions is representative of the entire paleo-oil reservoir, we suggest that the iron concretions present in the section can account for most, if not all, the iron that was removed from the red sandstone during bleaching. If we consider the inferred areal extent of the paleo-oil reservoir outlined in Figure 1 (~89.5 km²) and assume a density of 3,510 kg/m³ for Fe-oxide concretions, ~4,250,000 m³ of Fe_2O_3 is needed in total to balance the iron removed.

Given the observation of small Fe-oxide cubes in the yellow facies, and Fe-oxide concretions with pyrite cores, it is likely that most of the Fe-oxide concretions were originally pyrite and have since been oxidized (Figures 5b and 5f). The distinct homogeneity in both barite and pyrite sulfur isotope compositions among different grains and different analyses of the same grain suggest open-system conditions. If we assume that the barite in the red facies and the pyrite in the altered facies represent the same system, the magnitude of sulfur isotope fractionation is −12.1‰. The relatively small apparent fractionation (≤12.1‰) cannot be used to distinguish between thermochemical sulfate reduction (TSR; up to ~17‰; Meshoulam et al., 2016), and bacterial sulfate reduction (BSR; 2‰–66‰; Detmers et al., 2001; Sim et al., 2011). The presence of cubic post-pyrite and solid bitumen with high total sulfur contents suggests abiotic TSR (Anderson et al., 1987; Fisher & Hudson, 1987; Machel et al., 1995). However, we cannot discount BSR since the temperatures of middle Jurassic sandstones in the Paradox Basin did not reach higher than approximately 100°C (Nuccio & Condon, 1996). Most sulfate reducing microbes stop metabolizing above temperatures of ~80°C, whereas TSR is common in settings with temperatures higher than 100°C (Machel, 2001).

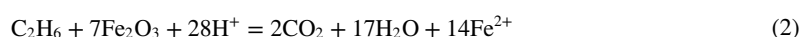
4.4. Geochemical Reactions

Reaction between the reduced, sulfur-containing hydrocarbons, associated acids, and red sandstone in our study area resulted in (a) the dissolution of iron-oxide grain coatings and K-feldspar (Figure 5a) and (b) the precipitation of pyrite (Figures 5b and 5f), quartz overgrowths, and authigenic illite (Figures 5b, 5d and 5e).

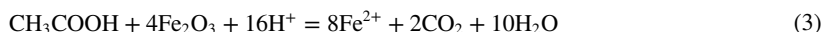
Iron-oxide dissolution (i.e., bleaching) reactions involving oil, acetic acid, and sulfur can be represented by the equations below (Equations 1–3; Chan et al., 2000; Eichhubl et al., 2009; Gorenc & Chan, 2015; Kampman et al., 2013; Parry et al., 2004). In the following reactions, we assume that the sulfur is sourced from the oil and use simplified chemical representations of oil.



for the reaction of sulfur-containing oil with hematite, forming acetic acid and pyrite,

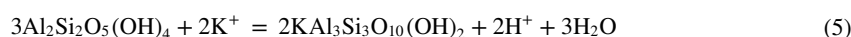
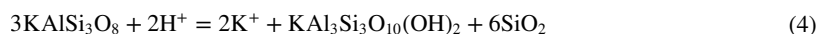


for the reaction of oil with hematite, forming CO₂ and ferrous iron, or



for the reaction of acetic acid produced in Equation 1 with hematite, forming CO₂ and ferrous iron.

The breakdown of K-feldspar is often attributed to acidity in the pore fluids formed from the production of CO₂ from reduction of iron-oxides (Equations 2 and 3), or the presence of acetic acid (Equations 1 and 3), and can be represented by Equation 4. This reaction also describes the precipitation of illite and quartz overgrowths. The presence of K⁺ ions formed in Equation 4 can also promote the illitization of kaolinite, as described in Equation 5.



The formation of illite from the breakdown of K-feldspar or kaolinite (Equations 4 and 5) can occur at temperatures of 120°C–140°C in a closed system (Bjørlykke & Aagaard, 1992). However, Wilkinson and Haszeldine (2002) suggest that fibrous illite growth is limited by nucleation kinetics rather than thermodynamic stability based on a lack of zero illite ages in present-day oil fields. Oil-charging, or the influx of acidic fluids, can create conditions that overcome this kinetic barrier to illite precipitation (Haszeldine et al., 2003; Wilkinson & Haszeldine, 2002). Further, conditions such as high K⁺/H⁺ activity ratios can promote illite precipitation and K⁺ can be derived from both K-feldspar dissolution (Equation 4) and external K-rich fluids (Lanson et al., 2002). However, some K-feldspar grains in our studied samples appear unaffected by dissolution (Figure 5a), and the overall K₂O concentrations of the clay-rich yellow facies are higher than in the presumed red-facies precursor (Figure 6a). This suggests an additional external source of K⁺ ions was available to promote illite precipitation. It has been proposed that illitization in the Rotliegend Sandstones of the North Sea occurred due to the influx of K-rich fluids derived from the Zechstein salt deposits (Lanson et al., 1996). Some of the K⁺ that allowed for the precipitation of significant fibrous pore-filling illite in our study could have been derived from K-rich formation waters that accompanied hydrocarbon migration.

4.5. Geochemical Modeling

Using PHREEQC, we performed a batch geochemical advection model to explore if the chemical interaction of a reduced fluid with a hematite-bearing sandstone produces the mineralogical changes we observe in the studied section. The phreeqc.dat database was used and amended to include acetate for our simulation.

4.5.1. Initial Conditions

Our sandstone was represented by one “cell” with 20% porosity containing fresh groundwater with the composition of fresh groundwater collected from the Jurassic Navajo sandstone (sample PW-8b) by J.-H. Kim et al. (2022). This initial groundwater is assumed to represent the composition of groundwater that was present in the Jurassic Entrada Sandstone prior to hydrocarbon infiltration. The temperature of the initial fluid was assumed to be 80°C, based on the proposed burial temperature of Jurassic formations at ~41 Ma (Nuccio & Condon, 1996). Point count and geochemical data were used to estimate the proportion of each mineral in the initial hematite-bearing sandstone (cell). The cell consisted of 83% quartz, 8% K-feldspar, 3.8% illite, 3% calcite, 1.5% plagioclase (0.75% anorthite and 0.75% albite), and 0.7% hematite.

4.5.2. Reducing Hydrocarbons and Associated Aqueous Brines

We used a combination of acetate, CH₄, and CO₂ to represent hydrocarbons or the anoxic degradation products of crude oil in our model. According to J.-H. Kim et al. (2022), the paleo-evaporated seawater-derived brines from the Pennsylvanian Honaker Trail and Paradox Formations are associated with hydrocarbons sourced from the Paradox Formation black shales. These brines were interpreted to be a major source of reduced fluids that were expelled during burial and bleached shallow red bed sandstones (J.-H. Kim et al., 2022). Based on these interpretations, we also assumed that migrating hydrocarbons were equilibrated with a reduced infiltrating fluid that had a composition equivalent to the paleo-evaporated seawater-derived brine collected from the Honaker Trail formation (Big Indian 24–31; J.-H. Kim et al., 2022). Prior to infiltration, the hydrocarbons and associated

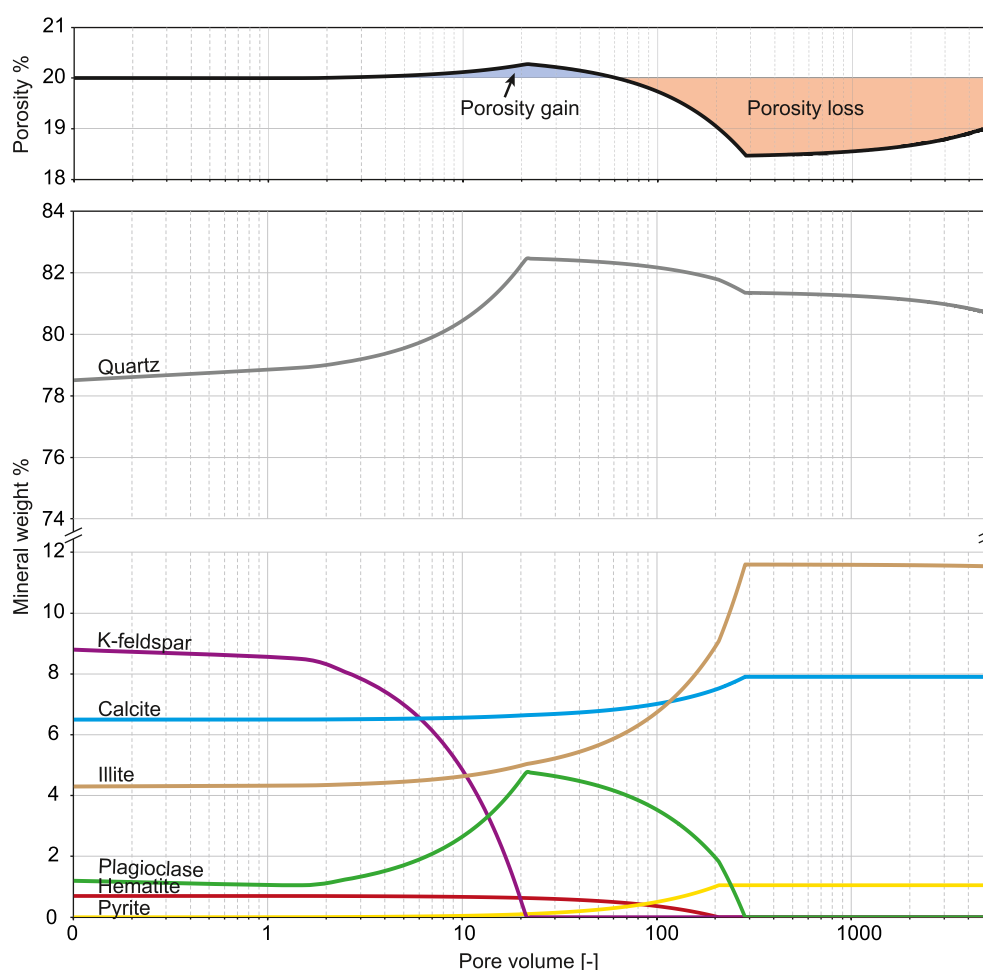


Figure 9. Modeling results showing the changing sandstone mineral assemblage with increasing pore volume (number of times the pore volume of the cell has been completely displaced by reduced fluid influx).

brines were first equilibrated with pyrite. The brine was assumed to have a temperature of 120°C, based off the burial temperature of Pennsylvanian-Permian formations at ~41 Ma (Nuccio & Condon, 1996).

4.5.3. Advection Simulation

We used an advection model simulating one-dimensional flow with reactions that assumes no dispersion or diffusion. With each step, the reduced hydrocarbon-bearing brine is advected into the cell consisting of the sandstone components and displaces the fluid that filled the pore volume of the cell in the prior step. The fluid and the cell chemically equilibrate during each step, altering the mineral assemblage if needed. Quartz, K-feldspar, plagioclase, calcite, illite, hematite and pyrite were allowed to dissolve or precipitate during the simulation. Eventually, the composition of the sandstone will be in equilibrium with that of the reduced infiltrating fluid. The number of pore volumes indicates how often the fluid in the pore volume of the cell is displaced by new influx of the reduced fluid. We modeled the advection of 5,000 pore volumes (Figure 9).

4.5.4. Model Results

Figure 9 shows the changing mineral assemblage (mineral weight %) and porosity of the sandstone as a function of increasing fluid-rock ratio as pore volume (increasing flux of reduced fluid). The most significant changes occur at fluid fluxes between about 2 and 200 pore-volumes. We observe K-feldspar dissolution occurring early in the simulation but most dissolution occurs between 2 and 20 pore volumes, at which point it is fully dissolved. Quartz starts to precipitate and reaches a maximum concentration at 20 pore volumes, similarly to plagioclase. After 20 pore volumes, both quartz and plagioclase start to dissolve. Quartz concentrations remain higher than the initial

values, despite some dissolution taking place, however, plagioclase is fully dissolved after ~300 pore volumes. Calcite and illite start to precipitate after approximately 10 pore volumes, and both reach a maximum and equilibrated concentration at 300 pore volumes. Illite increases from an initial 4.3%–11.5%, and calcite increases from 6.5% to 7.9%. Hematite starts to dissolve after approximately 20 pore volumes and is fully dissolved after 200 pore volumes. The dissolution of hematite is accompanied by the precipitation of pyrite, and a maximum pyrite concentration is reached once all hematite is dissolved.

The porosity of the sandstone initially increases by less than a percent, reaching a maximum coinciding with the full dissolution of K-feldspar. After this, porosity decreases, reaching a minimum of 18% at ~200 pore volumes as illite and calcite start to precipitate.

This simple batch geochemical model of the reaction between oxidized hematite-bearing sandstone and reduced hydrocarbon-bearing brine produces mineralogical results very similar to our observations from the sampled transect (Figure 3). These include quartz overgrowths, dissolved and heavily altered K-feldspar, calcite cement, pore-filling illite, and pyrite concretions. The illite mode increases from 3.8% to 11.5%, essentially the same (~12%) observed in the yellow facies. The model also suggests that the porosity of red bed sandstone increases during the initial phases of hydrocarbon migration (secondary porosity), but eventually decreases with continued reaction as illite and calcite fill pore spaces.

4.6. Confinement of the Bleached Horizon

The bleaching documented in our study is confined to a 27-m thick layer that is laterally consistent for at least 10 km. The gray facies that contains bitumen is 9 m thick, and where observed, does not step up or down stratigraphically. This raises the question of why oil migration and sandstone bleaching were confined to this specific horizon in a relatively homogenous section of the Entrada Sandstone. There are at least two explanations: (a) pre-existing porosity and mineralogical differences within the Slick Rock sandstone; or (b) reaction infiltration instabilities caused by fluid-rock interactions.

We observe a very thin silt layer at the interface between the upper yellow and pink facies (Figure 2). The low permeability and small pore throats of siltstone could be sufficient to form a capillary seal which would impede flow of hydrocarbons, if this silt layer were laterally continuous. Capillary seals form where the buoyancy force of the hydrocarbons is lower than the capillary pressure across pore throats. Although the silt layer is only on order millimeters thick, the height of the hydrocarbon column it can support are unrelated to the thickness of the seal layer itself, and instead is a function of the grain size and associated capillary pressure across pore throats (Ingram et al., 1997). Nonetheless, thinner seals are likely to vary laterally and are more easily breached by fractures or faults. The tar sand is mostly laminated in the upper half and displays syn-sedimentary deformation in the lower half, in contrast to the red, pink, and upper yellow facies that are cross-bedded (Figure 2). In general, the gray facies has more rounded grains than the other facies which create a higher permeability zone (Figure 2). Chan et al. (2000) suggested that heterogeneities in the deformed bedding of the gray facies caused the oil to remain trapped in the stratigraphic bound unit. In contrast to our observations, they suggested that the gray facies was a lower permeability tar-saturated sabkha deposit sandwiched between dune deposits (yellow facies). However, this then raises the question of why oil preferentially entered the lower permeability unit. Fryberger et al. (1983) suggests that organic-rich sabkha and interdune deposits within eolian systems are potential source rocks for hydrocarbon accumulations, where zones of early cementation provide local seals. Organic carbon contents up to 1.5% occur in the modern continental sabkha deposits of inland Egypt and the Arabian Gulf, where organic carbon is derived from algae and microbial mats that accumulated under saline and reducing conditions (Słowakiewicz et al., 2016; Zaki et al., 2011). However, accumulation of organic matter in these settings is thin and spatially heterogeneous, and a very high degree of organic matter degradation suggests very low preservation potential (Słowakiewicz et al., 2016). Also, organic carbon contents at our study site may be as high as ~8% based on loss-on-ignition.

An alternative hypothesis that caused oil migration to be confined to a specific horizon is the formation of a reaction infiltration instability. A reaction infiltration instability is formed when a scalloped reaction front forms spontaneously in a rock that starts with a homogeneous texture (Ortoleva et al., 1987). These spontaneous zones of enhanced porosity increase the local fluid flux, where the reactive solution eventually moves along high-permeability zones through the rock (Szymczak & Ladd, 2014). Increased fluid flux causes faster

dissolution, leading to a positive feedback cycle of increased fluid flow and enhanced dissolution. Dissolution of K-feldspar and pre-existing calcite cement that we observe in the yellow facies may have been sufficient to create localized zones of higher permeability. Our geochemical model also shows that porosity of the sandstone increases during the initial phases of oil migration, mostly due to K-feldspar dissolution. However, as shown on Figure 2, the sandstone is not fully homogeneous and does display variations in sorting, roundness, and bedding across the section. It is likely that a combination of factors including the top silt layer, well sorted and more rounded grains (Figure 2), and reaction infiltration instabilities played a role in confining oil migration to this horizon.

4.7. Mobilization of HFSE and Other Trace Elements

Early diagenetic iron oxide minerals have the potential to scavenge trace elements from interstitial aqueous solutions and control the redox chemistry of the sediment (Vesper, 2019). Iron-oxide grain coatings in red sandstones also act as a sorbent and host the majority of the mobile trace elements (Abdelouas et al., 1998; Beitler et al., 2005; Wigley et al., 2012). Therefore, dissolution of iron-oxide grain coatings could cause simultaneous removal of heavy trace elements into solution and explain reduced amounts of HFSE and other REE that we observe in the gray facies compared to the unaltered red facies (Figure 6e). For example, concentrations of TiO_2 decrease from an average of 1,250 ppm in the yellow facies and 1,100 ppm in the red facies, to as low as 590 ppm in the gray facies.

Under the relatively low temperature and pressure conditions of burial diagenesis, Ti is extremely insoluble and therefore often assumed to be immobile. However, there is abundant evidence, in addition to the authigenic titanium-bearing minerals observed in our study, that Ti is mobilized in the presence of organic acids (Hays et al., 1994; Parnell, 2004; Pe-Piper et al., 2011; Schulz et al., 2016; Sindern et al., 2019). Schulz et al. (2016) find anatase crystals along faults with hydrocarbon-bearing sandstones, and at oil-water contacts in oilfields. Authigenic Ti minerals such as anatase and brookite are subsequently precipitated upon decay of organo-titanium complexes and oxidation of organic matter, and therefore can mark the change from a reducing to oxidizing regime (Hays et al., 1994; Pe-Piper et al., 2011; Schulz et al., 2016; Sindern et al., 2019). Morad (1988) suggests that dissolution and precipitation of Ti takes place on a cm-scale because Ti^{4+} ions can only be mobilized short distances. Our observation of higher HFSE and Ti concentrations in the yellow facies, combined with the presence of authigenic brookite/anatase crystals in the yellow and gray facies (Figures 5a, 5d and 5e), suggests localized redistribution of these elements. We suggest that the migration of hydrocarbons and dissolution of iron-oxide grain coatings caused the removal of HFSE and REE in the gray facies. The dissolved HFSE were then locally reprecipitated into the adjacent yellow facies.

4.8. Late Enrichment of Cu and U

Uranium concentrations are higher by a factor of two in the gray facies, and a factor of nine in the concretions. Copper is enriched by a greater extent – up to a factor of seven in the gray facies and 37 in the concretions. Vanadium is enriched by only ~1.2 to 2× in the yellow, pink, and gray facies but by a factor of 13 in the concretions. Overall, concentrations of Cu, U, and V are higher in all the altered facies and concretions, in contrast to other elements such as Fe, Mg, and Mn that are depleted in the gray facies but enriched in concretions, when compared to the red facies (Figures 4c and 4f).

The Paradox Basin hosts a number of fault-controlled sediment hosted stratiform copper deposits, such as at Cashin (MacIntyre, 2006) and Lisbon Valley mines (Hahn & Thorson, 2005), and sandstone-hosted U ± V deposits such as the Salt Wash member of the Morrison formation in the Uravan mineral belt (Barton et al., 2018; Chenoweth, 1981). The Cu-sulfide and U ± V deposits at these locations are both associated with bleached sandstones and the presence of pyrite, bitumen, or carbonaceous fossil plant material (Breit & Meunier, 1990; Hahn & Thorson, 2005; Hitzman et al., 2005; Morrison & Parry, 1986). The solubility of U and V are controlled by redox state and are generally mobilized in oxidizing fluids (e.g., Barton et al., 2018). Copper behaves similarly but depends more on chloride content as well as the presence of sulfide (Barton et al., 2018). It has been proposed that widespread bleaching of red sandstones and local pyrite precipitation was caused by reducing hydrocarbon-bearing fluids prior to copper and uranium mineralization in the Paradox Basin (Hahn & Thorson, 2005; Thorson, 2004, 2018; Whitehead, 2019). Thorson (2018) suggests that after the formation of a

reductant trap, such as hydrocarbons trapped in pore throats, oxidized, saline brines carrying Cu, U, V, and other trace elements utilized earlier fluid conduits and deposited minerals such as Cu-sulfides that replaced earlier pyrite, bitumen, or other organic material. It is generally hypothesized that the oxidized fluid is younger than the alteration caused by flow of hydrocarbon-bearing fluids (Hitzman et al., 2005; Thorson, 2018).

Our observation of higher concentrations of Cu, U, and V, as well as azurite concretions in some locations, in the gray bitumen-saturated sandstone, are consistent with a model of late Cu and U/V enrichment in previously reduced and bleached rocks. Interestingly, these elements are enriched in almost all the altered facies in addition to the Fe-bearing concretions, in contrast with depletions from the gray sandstone and local enrichment for elements like Fe and HFSE in Fe-concretions (Figures 6c and 6e). This may support transport of Cu, U, and V into the Slick Rock sandstone from an external source. By weighting the Cu, U, and V concentrations to the thicknesses of each facies, and assuming the initial concentration in the entire section was equivalent to that of the red facies, 1.6–2.1× of Cu, 0.6–0.7× of U, and 0.1–0.8× of V has been gained in the section. This does not include the additional concentrations of Cu, U, and V hosted in the concretions. This suggests significant mass influx of these elements from external sources in an open hydrological system.

5. Conclusions

Sandstones altered by the flow of hydrocarbons at Rainbow Rocks offer valuable insights into the geochemical and mineralogical consequences of fluid-rock interactions associated with petroleum migration and storage. The presence of bitumen in the pore spaces of the altered gray facies, and comparison of compositional and mineralogic gradients with the batch geochemical model, are consistent with hydrocarbon migration as the primary cause of variations in sandstone colors, major and trace element variations, and mineralogic changes through the section.

In summary, hydrocarbon migration resulted in: (a) complete dissolution of iron-oxide grain coatings; (b) formation of quartz overgrowths; (c) dissolution of K-feldspar and initial increase in porosity; and (d) precipitation of fine-grained authigenic clays, calcite cement, euhedral anatase/brookite, pyrite concretions and subsequent decrease in porosity. Fe_2O_3 concentrations were reduced by more than a factor of three in the central part of the hydrocarbon flow zone, but locally enriched up to $\sim 50\times$ (~ 30 wt.% Fe_2O_3) in iron-concretions that likely accommodated most of the dissolved iron. The reduced fluids were also responsible for the localized redistribution of other metals such as Zn, Pb, REE, and HFSE that also have lowest concentrations in the gray facies, but highest in the concretions. Localized redistribution of iron can account for most of the iron removed during bleaching, suggesting minimal long-distance transport of Fe-bearing reduced fluids. Al_2O_3 and K_2O concentrations are highest at the boundary between the yellow and pink facies, coinciding with the highest clay concentrations and lowest porosity. We also observe authigenic clay particles intergrown with bitumen in some pore spaces of the gray facies.

Calcite cement in the gray facies has a more negative $\delta^{13}\text{C}$ signature than calcite in the unaltered red facies and precipitated from a hybrid source of groundwater and hydrocarbons. Compiled carbonate isotopic compositions show that most cement in bleached sandstones across the Paradox Basin precipitated from a mixture of paleo-evaporated seawater derived brines from the Pennsylvanian Paradox Formation and fresh meteoric-derived groundwater. The hydrocarbons responsible for bleaching the Entrada Sandstone in our study area was sulfur-rich and likely sourced from the Paradox formation. The oil migrated up the Courthouse Fault and into the Entrada Sandstone ~ 41 Ma (Bailey et al., 2022). Bleaching of the sandstone, accumulation of bitumen in pore spaces, and pyrite precipitation formed a reducing trap required for Cu, U, and V deposition from the flow of younger, oxidized saline brines.

Data Availability Statement

All the data produced for this study (point counting, bulk geochemistry, stable isotopes, and PHREEQC model results) are available on Dataverse via <https://doi.org/10.7910/DVN/HDT67J>. The PHREEQC code written for the geochemical modeling portion of this study is also available in the data repository. Version 3 of PHREEQC is open source and available via <https://www.usgs.gov/software/phreeqc-version-3>.

Acknowledgments

Funding for this research was provided by the William F. Keck Foundation, the National Science Foundation-Division of Earth Sciences (Grant #2120733), the Swedish Research Council (#2017-05186 and #2021-04365), the Formas (#2020-01577), and the Crafoord Foundation (#20210524). The authors acknowledge Peter Mozley for introducing Rainbow Rocks, and Margie Chan and David Loope for many helpful discussions about red-bed bleaching and fluid-rock reaction. The authors thank Dennis Newell for assistance with PHREEQC. The authors also acknowledge Dr. Uttam Chowdhury, Sean Callahan, and Kerstin Lindén for sample preparation and analytical assistance. The authors thank the reviewers for their comments that greatly improved the manuscript. This is NordSIMS publication #717.

References

- Abdelouas, A., Lu, Y., Lutze, W., & Nuttall, H. E. (1998). Reduction of U(VI) to U(IV) by indigenous bacteria in contaminated ground water. *Journal of Contaminant Hydrology*, 35(1–3), 217–233. [https://doi.org/10.1016/s0169-7722\(98\)00134-x](https://doi.org/10.1016/s0169-7722(98)00134-x)
- Anderson, T. F., Kruger, J., & Raiswell, R. (1987). C-S-Fe relationships and the isotopic composition of pyrite in the New Albany Shale of the Illinois Basin, U.S.A. *Geochimica et Cosmochimica Acta*, 51(10), 2795–2805. [https://doi.org/10.1016/0016-7037\(87\)90159-1](https://doi.org/10.1016/0016-7037(87)90159-1)
- Bailey, L. R., Kirk, J., Hemming, S. R., Krantz, R. W., & Reiners, P. W. (2022). Eocene fault-controlled fluid flow and mineralization in the Paradox Basin, United States. *Geology*, 50(3), 326–330. <https://doi.org/10.1130/G49466.1>
- Barth, T., & Björlykke, K. (1993). Organic acids from source rock maturation: Generation potentials, transport mechanisms and relevance for mineral diagenesis. *Applied Geochemistry*, 8(4), 325–337. [https://doi.org/10.1016/0883-2927\(93\)90002-X](https://doi.org/10.1016/0883-2927(93)90002-X)
- Barton, I. F., Barton, M. D., & Thorson, J. P. (2018). Characteristics of Cu and U-V deposits in the Paradox Basin (Colorado Plateau) and associated alteration. *Society of Economic Geologists Guidebook Series*, 59, 30.
- Beitler, B., Chan, M. A., & Parry, W. T. (2003). Bleaching of Jurassic Navajo Sandstone on Colorado Plateau Laramide highs: Evidence of exhumed hydrocarbon supergiants? *Geology*, 31(12), 1041. <https://doi.org/10.1130/G19794.1>
- Beitler, B., Parry, W. T., & Chan, M. A. (2005). Fingerprints of fluid flow: Chemical diagenetic history of the Jurassic Navajo Sandstone, Southern Utah, U.S.A. *Journal of Sedimentary Research*, 75(4), 547–561. <https://doi.org/10.2110/jsr.2005.045>
- Bergman, S. C., Huntington, K. W., & Crider, J. G. (2013). Tracing paleofluid sources using clumped isotope thermometry of diagenetic cements along the Moab Fault, Utah. *American Journal of Science*, 313(5), 490–515. <https://doi.org/10.2475/05.2013.03>
- Björlykke, K., & Aagaard, P. (1992). Clay minerals in North Sea sandstones. In D. W. Houseknecht & E. D. Pittman (Eds.), *Origin, diagenesis, and petrophysics of clay minerals in sandstones* (pp. 65–80). SEPM (Society for Sedimentary Geology). <https://doi.org/10.2110/pec.92.47>
- Breit, G. N. (1986). *Geochemical study of authigenic minerals in the Salt Wash member of the Morrison formation, Slick Rock district, San Miguel County, Colorado* (Doctoral dissertation). Colorado School of Mines. Retrieved from <https://www.osti.gov/biblio/6278322-geochemical-study-authigenic-minerals-salt-wash-member-morrison-formation-slick-rock-district-san-miguel-county-colorado>
- Breit, G. N., & Meunier, J.-D. (1990). Fluid inclusion, delta ¹⁸O, and ⁸⁷Sr/⁸⁶Sr evidence for the origin of fault-controlled copper mineralization, Lisbon Valley, Utah, and Slick Rock District, Colorado. *Economic Geology*, 85(4), 884–891. <https://doi.org/10.2113/gsecongeo.85.4.884>
- Chan, M. A., Ormö, J., Park, A. J., Stich, M., Souza-Egipsy, V., & Komatsu, G. (2007). Models of iron oxide concretion formation: Field, numerical, and laboratory comparisons. *Geofluids*, 7(3), 356–368. <https://doi.org/10.1111/j.1468-8123.2007.00187.x>
- Chan, M. A., Parry, W. T., & Bowman, J. R. (2000). Diagenetic hematite and manganese oxides and fault-related fluid flow in Jurassic Sandstones, Southeastern Utah. *AAPG Bulletin*, 84(9), 1281–1310. <https://doi.org/10.1306/A9673E82-1738-11D7-8645000102C1865D>
- Chan, M. A., Parry, W. T., Petersen, E. U., & Hall, C. M. (2001). ⁴⁰Ar/³⁹Ar age and chemistry of manganese mineralization in the Moab and Lisbon fault systems, southeastern Utah. *Geology*, 29(4), 331–334. [https://doi.org/10.1130/0091-7613\(2001\)029<0331:aaaaco>2.0.co;2](https://doi.org/10.1130/0091-7613(2001)029<0331:aaaaco>2.0.co;2)
- Chenoweth, W. L. (1981). Uranium-vanadium deposits of the Uravan mineral belt and adjacent areas, Colorado and Utah. *Field Conference Guidebook*, 32, CONF-8110216-. Retrieved from <https://www.osti.gov/biblio/5541410>
- Chidsey, T. C. (2009). *Major oil plays in Utah and vicinity: Final report*. Utah Geological Survey.
- Coplen, T. B. (1994). Reporting of stable hydrogen, carbon, and oxygen isotopic abundances (Technical Report). *Pure and Applied Chemistry*, 66(2), 273–276. <https://doi.org/10.1351/pac199466020273>
- Detmers, J., Brückert, V., Habicht, K. S., & Kuever, J. (2001). Diversity of sulfur isotope fractionations by sulfate-reducing prokaryotes. *Applied and Environmental Microbiology*, 67(2), 888–894. <https://doi.org/10.1128/AEM.67.2.888-894.2001>
- Dickinson, W. R. (1970). Interpreting detrital modes of graywacke and arkose. *Journal of Sedimentary Research*, 40(2), 695–707. <https://doi.org/10.1306/74D72018-2B21-11D7-8648000102C1865D>
- Dickinson, W. R. (1988). Provenance and sediment dispersal in relation to paleotectonics and paleogeography of sedimentary basins. In K. L. Kleinspehn & C. Paola (Eds.), *New perspectives in basin analysis* (pp. 3–25). Springer. https://doi.org/10.1007/978-1-4612-3788-4_1
- Ding, T., Valkiers, S., Kipphardt, H., De Bièvre, P., Taylor, P. D. P., Gonfiantini, R., & Krouse, R. (2001). Calibrated sulfur isotope abundance ratios of three IAEA sulfur isotope reference materials and V-CDT with a reassessment of the atomic weight of sulfur. *Geochimica et Cosmochimica Acta*, 65(15), 2433–2437. [https://doi.org/10.1016/S0016-7037\(01\)00611-1](https://doi.org/10.1016/S0016-7037(01)00611-1)
- Doelling, H. H. (2002). *Geologic map of the Moab and eastern part of the San Rafael Desert 30' x 60' Quadrangles, Grand and Emery Counties, Utah, and Mesa County, Colorado* [Map]. Utah Geological Survey.
- Drake, H., Åström, M. E., Heim, C., Broman, C., Åström, J., Whitehouse, M., et al. (2015). Extreme ¹³C depletion of carbonates formed during oxidation of biogenic methane in fractured granite. *Nature Communications*, 6(1), 7020. <https://doi.org/10.1038/ncomms8020>
- Drake, H., Whitehouse, M. J., Heim, C., Reiners, P. W., Tillberg, M., Hogmalm, K. J., et al. (2018). Unprecedented ³⁴S-enrichment of pyrite formed following microbial sulfate reduction in fractured crystalline rocks. *Geobiology*, 16(5), 556–574. <https://doi.org/10.1111/gbi.12297>
- Eichhubl, P., Davatzes, N. C., & Becker, S. P. (2009). Structural and diagenetic control of fluid migration and cementation along the Moab fault, Utah. *AAPG Bulletin*, 93(5), 653–681. <https://doi.org/10.1306/02180908080>
- Fisher, I. S. J., & Hudson, J. D. (1987). Pyrite formation in Jurassic shales of contrasting biofacies. *Geological Society, London, Special Publications*, 26(1), 69–78. <https://doi.org/10.1144/GSL.SP.1987.026.01.04>
- Fryberger, S. G., Al-Sari, A. M., & Clisham, T. J. (1983). Eolian dune, interdune, sand sheet, and siliciclastic sabkha sediments of an offshore prograding sand sea, Dhahran Area, Saudi Arabia. *AAPG Bulletin*, 67(2), 280–312. <https://doi.org/10.1306/03B5ACFF-16D1-11D7-8645000102C1865D>
- Garcia, V. H., Reiners, P. W., Shuster, D. L., Idleman, B., & Zeitler, P. K. (2018). Thermochronology of sandstone-hosted secondary Fe- and Mn-oxides near Moab, Utah: Record of paleo-fluid flow along a fault. *GSA Bulletin*, 130(1–2), 93–113. <https://doi.org/10.1130/B31627.1>
- Garden, I. R., Guscott, S. C., Burley, S. D., Foxford, K. A., Walsh, J. J., & Marshall, J. (2001). An exhumed palaeo-hydrocarbon migration fairway in a faulted carrier system, Entrada Sandstone of SE Utah, USA. *Geofluids*, 1(3), 195–213. <https://doi.org/10.1046/j.1468-8123.2001.00018.x>
- Gerrild, P. M. (1976). A geochemical study of oil in metalliferous veins, Idarado Mine, San Juan Mountains, Colorado. *Journal of Research of the U. S. Geological Survey*, 4(5), 593–599.
- Gorenc, M. A., & Chan, M. A. (2015). Hydrocarbon-induced diagenetic alteration of the Permian White Rim Sandstone, Elaterite Basin, south-east Utah. *AAPG Bulletin*, 99(05), 807–829. <https://doi.org/10.1306/10081413128>
- Hahn, G. A., & Thorson, J. P. (2005). Geology of the Lisbon valley sandstone-hosted disseminated copper deposits, San Juan County, Utah. In J. P. Thorson (Ed.), *Lisbon valley sediment-hosted copper deposits and Paradox Basin fluids trip*. Society of Economic Geologists. <https://doi.org/10.5382/GB.37.ch3>
- Harrison, A. G., & Thode, H. G. (1958). Sulphur isotope abundances in hydrocarbons and source rocks of Uinta Basin, Utah. *AAPG Bulletin*, 42. <https://doi.org/10.1306/0BDA5C00-16BD-11D7-8645000102C1865D>
- Haszeldine, R. S., Cavanagh, A. J., & England, G. L. (2003). Effects of oil charge on illite dates and stopping quartz cement: Calibration of basin models. *Journal of Geochemical Exploration*, 78(79), 373–376. [https://doi.org/10.1016/S0375-6742\(03\)00151-1](https://doi.org/10.1016/S0375-6742(03)00151-1)

- Hays, P. D., James, W. D., & Tieh, T. T. (1994). The role of NAA in studies of organic diagenesis of rocks. *Journal of Radioanalytical and Nuclear Chemistry Articles*, 180(1), 15–23. <https://doi.org/10.1007/BF02039897>
- Heinonen, A., Andersen, T., Rämö, O. T., & Whitehouse, M. (2015). The source of Proterozoic anorthosite and rapakivi granite magmatism: Evidence from combined in situ Hf–O isotopes of zircon in the Ahvenisto complex, southeastern Finland. *Journal of the Geological Society*, 172(1), 103–112. <https://doi.org/10.1144/jgs2014-013>
- Hintze, L. F., Willis, G. C., Laes, D. Y. M., Sprinkle, D. A., & Brown, K. D. (2000). *Digital geologic map of Utah*. Utah Geological Survey. <https://doi.org/10.34191/M-179DM>
- Hitzman, M., Kirkham, R., Broughton, D., Thorson, J., & Selley, D. (2005). The Sediment-hosted stratiform copper ore system. In J. W. Hedenquist, J. F. H. Thompson, R. J. Goldfarb, & J. P. Richards (Eds.), *One hundredth anniversary volume*. Society of Economic Geologists. <https://doi.org/10.5382/AV100.19>
- Hodson, K. R., Crider, J. G., & Huntington, K. W. (2016). Temperature and composition of carbonate cements record early structural control on cementation in a nascent deformation band fault zone: Moab Fault, Utah, USA. *Tectonophysics*, 690, 240–252. <https://doi.org/10.1016/j.tecto.2016.04.032>
- Huntoon, J. E., Hansley, P. L., & Naeser, N. D. (1999). The search for a source rock for the giant tar sand triangle accumulation, southeastern Utah. *AAPG Bulletin*, 83(3), 467–495. <https://doi.org/10.1306/00AA9BD8-1730-11D7-8645000102C1865D>
- Ingersoll, R. V., Bullard, T. F., Ford, R. L., Grimm, J. P., Pickle, J. D., & Sares, S. W. (1984). The effect of grain size on detrital modes: A test of the Gazzi-Dickinson point-counting method. *Journal of Sedimentary Research*, 54(1), 103–116. <https://doi.org/10.1306/212F83B9-2B24-11D7-8648000102C1865D>
- Ingram, G. M., Urai, J. L., & Naylor, M. A. (1997). Seal processes and top seal assessment. In P. Möller-Pederson & A. G. Koestler (Eds.), *Hydrocarbon seals: Importance for exploration and production* (pp. 165–174).
- Jensen, M. L. (1958). Sulfur isotopes and the origin of sandstone-type uranium deposits [Colorado Plateau and Wyoming]. *Economic Geology*, 53(5), 598–616. <https://doi.org/10.2113/gsecongeo.53.5.598>
- Johnson, D. M., Hooper, P. R., & Conrey, R. M. (1999). *XRF analysis of rocks and minerals for major and trace elements on a single low dilution Li-tetraborate fused bead*. JCPDS-International Centre for Diffraction Data.
- Kamber, B. S., & Whitehouse, M. J. (2007). Micro-scale sulphur isotope evidence for sulphur cycling in the late Archean shallow ocean. *Geobiology*, 5(1), 5–17. <https://doi.org/10.1111/j.1472-4669.2006.00091.x>
- Kampman, N., Maskell, A., Bickle, M. J., Evans, J. P., Schaller, M., Purser, G., et al. (2013). Scientific drilling and downhole fluid sampling of a natural CO₂ reservoir, Green River, Utah. *Scientific Drilling*, 16, 33–43. <https://doi.org/10.5194/sd-16-33-2013>
- Kim, J.-H., Bailey, L., Noyes, C., Tyne, R. L., Ballentine, C. J., Person, M., et al. (2022). Hydrogeochemical evolution of formation waters responsible for sandstone bleaching and ore mineralization in the Paradox Basin, Colorado Plateau, USA. *GSA Bulletin*. <https://doi.org/10.1130/B36078.1>
- Kim, S.-T., & O'Neil, J. R. (1997). Equilibrium and nonequilibrium oxygen isotope effects in synthetic carbonates. *Geochimica et Cosmochimica Acta*, 61(16), 3461–3475. [https://doi.org/10.1016/S0016-7037\(97\)00169-5](https://doi.org/10.1016/S0016-7037(97)00169-5)
- Kirkland, D. W., Denison, R. E., & Rooney, M. A. (1995). Diagenetic alteration of Permian strata at oil fields of south central Oklahoma, USA. *Marine and Petroleum Geology*, 12(6), 629–644. [https://doi.org/10.1016/0264-8172\(95\)98089-N](https://doi.org/10.1016/0264-8172(95)98089-N)
- Lanson, B., Beaufort, D., Berger, G., Baradat, J., & Lachapagne, J.-C. (1996). Illitization of diagenetic kaolinite-to-dickite conversion series: Late-stage diagenesis of the Lower Permian Rotliegend Sandstone reservoir, offshore of The Netherlands. *Journal of Sedimentary Research*, 66(3), 501–518.
- Lanson, B., Beaufort, D., Berger, G., Bauer, A., Cassagnabère, A., & Meunier, A. (2002). Authigenic kaolin and illitic minerals during burial diagenesis of sandstones: A review. *Clay Minerals*, 37(1), 1–22. <https://doi.org/10.1180/0009855023710014>
- Lee, M., Aronson, J. L., & Savin, S. M. (1989). Timing and conditions of Permian Rotliegend Sandstone Diagenesis, Southern North Sea: K/Ar and oxygen isotopic data. *AAPG Bulletin*, 73. <https://doi.org/10.1306/703C9B0E-1707-11D7-8645000102C1865D>
- Lewan, M. D., & Fisher, J. B. (1994). Organic acids from petroleum source rocks. In E. D. Pittman & M. D. Lewan (Eds.), *Organic acids in geological processes* (pp. 70–114). Springer Berlin Heidelberg. https://doi.org/10.1007/978-3-642-78356-2_4
- Liseroudi, M. H., Ardakani, O. H., Sanei, H., Pedersen, P. K., Stern, R. A., & Wood, J. M. (2020). Origin of sulfate-rich fluids in the Early Triassic Montney Formation, Western Canadian Sedimentary Basin. *Marine and Petroleum Geology*, 114, 104236. <https://doi.org/10.1016/j.marpetgeo.2020.104236>
- Loope, D. B., & Kettler, R. M. (2015). The footprints of ancient CO₂-driven flow systems: Ferrous carbonate concretions below bleached sandstone. *Geosphere*, 11(3), 943–957. <https://doi.org/10.1130/GES01094.1>
- Loope, D. B., Kettler, R. M., & Weber, K. A. (2010). Follow the water: Connecting a CO₂ reservoir and bleached sandstone to iron-rich concretions in the Navajo Sandstone of south-central Utah, USA. *Geology*, 38(11), 999–1002. <https://doi.org/10.1130/G31213.1>
- Loope, D. B., Kettler, R. M., & Weber, K. A. (2011). Morphologic clues to the origins of iron oxide-cemented spheroids, boxworks, and pipe-like concretions, Navajo Sandstone of south-central Utah, U.S.A. *The Journal of Geology*, 119(5), 505–520. <https://doi.org/10.1086/661110>
- Loope, D. B., Kettler, R. M., Weber, K. A., Hinrichs, N. L., & Burgess, D. T. (2012). Rind iron-oxide concretions: Hallmarks of altered siderite masses of both early and late diagenetic origin. *Sedimentology*, 59(6), 1769–1781. <https://doi.org/10.1111/j.1365-3091.2012.01325.x>
- Machel, H. G. (2001). Bacterial and thermochemical sulfate reduction in diagenetic settings—Old and new insights. *Sedimentary Geology*, 140(1–2), 143–175. [https://doi.org/10.1016/S0037-0738\(00\)00176-7](https://doi.org/10.1016/S0037-0738(00)00176-7)
- Machel, H. G., Krouse, H. R., & Sassen, R. (1995). Products and distinguishing criteria of bacterial and thermochemical sulfate reduction. *Applied Geochemistry*, 10(4), 373–389. [https://doi.org/10.1016/0883-2927\(95\)00008-8](https://doi.org/10.1016/0883-2927(95)00008-8)
- MacIntyre, T. J. (2006). *Fault-controlled hydrocarbon-related bleaching and sediment-hosted copper mineralization of the Jurassic Wingate Sandstone at the Cashin mine, Montrose County, Colorado* (Doctoral dissertation). Colorado School of Mines. Retrieved from <https://repository.mines.edu/handle/11124/79156>
- Meshoulam, A., Ellis, G. S., Said Ahmad, W., Deev, A., Sessions, A. L., Tang, Y., et al. (2016). Study of thermochemical sulfate reduction mechanism using compound specific sulfur isotope analysis. *Geochimica et Cosmochimica Acta*, 188, 73–92. <https://doi.org/10.1016/j.gca.2016.05.026>
- Morad, S. (1988). Diagenesis of titaniferous minerals in Jurassic sandstones from the Norwegian Sea. *Sedimentary Geology*, 57(1–2), 17–40. [https://doi.org/10.1016/0037-0738\(88\)90016-4](https://doi.org/10.1016/0037-0738(88)90016-4)
- Morrison, S. J., & Parry, W. T. (1986). Formation of carbonate-sulfate veins associated with copper ore deposits from saline basin brines, Lisbon Valley, Utah; fluid inclusion and isotopic evidence. *Economic Geology*, 81(8), 1853–1866. <https://doi.org/10.2113/gsecongeo.81.8.1853>
- Nuccio, V. F., & Condon, S. M. (1996). Burial and thermal history of the Paradox Basin, Utah and Colorado, and petroleum potential of the middle Pennsylvanian Paradox Formation. *U.S. Geological Survey Bulletin 2000-O*, 40.

- Ortoleva, P., Chadam, J., Merino, E., & Sen, A. (1987). Geochemical self-organization II: The reactive-infiltration instability. *American Journal of Science*, 287(10), 1008–1040. <https://doi.org/10.2475/ajs.287.10.1008>
- Parnell, J. (2004). Titanium mobilization by hydrocarbon fluids related to sill intrusion in a sedimentary sequence, Scotland. *Ore Geology Reviews*, 24(1–2), 155–167. <https://doi.org/10.1016/j.oregeorev.2003.08.010>
- Parry, W. T., Chan, M. A., & Beitle, B. (2004). Chemical bleaching indicates episodes of fluid flow in deformation bands in sandstone. *AAPG Bulletin*, 88(2), 175–191. <https://doi.org/10.1306/09090303034>
- Pe-Piper, G., Karim, A., & Piper, D. J. W. (2011). Authigenesis of titania minerals and the mobility of Ti: New evidence from pro-deltaic sandstones, Cretaceous Scotian Basin, Canada. *Journal of Sedimentary Research*, 81(10), 762–773. <https://doi.org/10.2110/jsr.2011.63>
- Potter-McIntyre, S., Allen, J., Lee, S.-Y., Han, W. S., Chan, M., & McPherson, B. (2013). Iron precipitation in a natural CO₂ reservoir: Jurassic Navajo Sandstone in the northern San Rafael Swell, UT, USA. *Geofluids*, 13(1), 82–92. <https://doi.org/10.1111/gfl.12014>
- Purser, G., Rochelle, C. A., Rushton, J., Pearce, J. M., & Wagner, D. (2014). An experimental and analogue study of iron release from red sandstones. *Energy Procedia*, 63, 3268–3274. <https://doi.org/10.1016/j.egypro.2014.11.354>
- Schulz, H.-M., Wirth, R., & Schreiber, A. (2016). Nano-crystal formation of TiO₂ polymorphs brookite and anatase due to organic–Inorganic rock–fluid interactions. *Journal of Sedimentary Research*, 86(2), 59–72. <https://doi.org/10.2110/jsr.2016.1>
- Schumacher, D. (1996). Hydrocarbon-induced alteration of soils and sediments. In D. Schumacher & M. A. Abrams (Eds.), *Hydrocarbon migration and its near-surface expression*. American Association of Petroleum Geologists. <https://doi.org/10.1306/M66606C6>
- Shalaby, M. R., Hakimi, M. H., & Abdullah, W. H. (2012). Geochemical characterization of solid bitumen (migrabitumen) in the Jurassic sandstone reservoir of the Tut Field, Shushan Basin, northern Western Desert of Egypt. *International Journal of Coal Geology*, 100, 26–39. <https://doi.org/10.1016/j.coal.2012.06.001>
- Sim, M. S., Bosak, T., & Ono, S. (2011). Large sulfur isotope fractionation does not require disproportionation. *Science*, 333(6038), 74–77. <https://doi.org/10.1126/science.1205103>
- Sindern, S., Havenith, V., Gerdes, A., Meyer, F. M., Adelman, D., & Hellmann, A. (2019). Dating of anatase-forming diagenetic reactions in Rotliegendes sandstones of the North German Basin. *International Journal of Earth Sciences*, 108(4), 1275–1292. <https://doi.org/10.1007/s00531-019-01705-x>
- Ślowski, M., Whitaker, F., Thomas, L., Tucker, M. E., Zheng, Y., Gedl, P., & Pancost, R. D. (2016). Biogeochemistry of intertidal microbial mats from Qatar: New insights from organic matter characterisation. *Organic Geochemistry*, 102, 14–29. <https://doi.org/10.1016/j.orggeochem.2016.09.006>
- Szymczak, P., & Ladd, A. J. C. (2014). Reactive-infiltration instabilities in rocks. Part 2. Dissolution of a porous matrix. *Journal of Fluid Mechanics*, 738, 591–630. <https://doi.org/10.1017/jfm.2013.586>
- Thorson, J. P. (2004). Paradox Basin sandstone-hosted copper deposits generated by two episodes of basinal fluid expulsion. *Geological Society of America, Abstracts with Programs*, 36, 517.
- Thorson, J. P. (2018). Paradox Basin fluids and Colorado Plateau copper, uranium, and vanadium deposits: Overview. *Society of Economic Geologists Guidebook Series*, 59, 13–46.
- Vesper, D. J. (2019). Contamination of cave waters by heavy metals. In W. B. White, D. C. Culver, & T. Pipan (Eds.), *Encyclopedia of caves* (3rd ed., pp. 320–325). Academic Press. <https://doi.org/10.1016/B978-0-12-814124-3.00035-2>
- Walker, T. R., Larson, E. E., & Hoblitt, R. P. (1981). Nature and origin of hematite in the Moenkopi Formation (Triassic), Colorado Plateau: A contribution to the origin of magnetism in red beds. *Journal of Geophysical Research*, 86(B1), 317. <https://doi.org/10.1029/JB086iB01p0317>
- Watson, J. S., Jones, D. M., Swannell, R. P. J., & van Duin, A. C. T. (2002). Formation of carboxylic acids during aerobic biodegradation of crude oil and evidence of microbial oxidation of hopanes. *Organic Geochemistry*, 33(10), 1153–1169. [https://doi.org/10.1016/S0146-6380\(02\)00086-4](https://doi.org/10.1016/S0146-6380(02)00086-4)
- Whitehead, A. (2019). *Comparison of sediment-hosted Cu mineralization Lisbon and Moab Fault Systems, Utah* (Master's thesis). The University of Arizona. Retrieved from <http://hdl.handle.net/10150/634336>
- Whitehouse, M. J. (2013). Multiple sulfur isotope determination by SIMS: Evaluation of reference sulfides for $\Delta^{33}\text{S}$ with observations and a case study on the determination of $\Delta^{36}\text{S}$. *Geostandards and Geoanalytical Research*, 37(1), 19–33. <https://doi.org/10.1111/j.1751-908X.2012.00188.x>
- Wigley, M., Dubacq, B., Kampman, N., & Bickle, M. (2013). Controls of sluggish, CO₂-promoted, hematite and K-feldspar dissolution kinetics in sandstones. *Earth and Planetary Science Letters*, 362, 76–87. <https://doi.org/10.1016/j.epsl.2012.11.045>
- Wigley, M., Kampman, N., Dubacq, B., & Bickle, M. (2012). Fluid-mineral reactions and trace metal mobilization in an exhumed natural CO₂ reservoir, Green River, Utah. *Geology*, 40(6), 555–558. <https://doi.org/10.1130/G32946.1>
- Wilkinson, M., & Haszeldine, R. S. (2002). Fibrous illite in oilfield sandstones – A nucleation kinetic theory of growth. *Terra Nova*, 14(1), 56–60. <https://doi.org/10.1046/j.1365-3121.2002.00388.x>
- Wilkinson, M., Haszeldine, R. S., & Fallick, A. E. (2006). Hydrocarbon filling and leakage history of a deep geopressured sandstone, Fulmar Formation, United Kingdom North Sea. *AAPG Bulletin*, 90(12), 1945–1961. <https://doi.org/10.1306/06270605178>
- Womer, M. B. (1986). Hydrocarbon Occurrence and Diagenetic History within Proterozoic Sediments, McArthur River Area, Northern Territory, Australia. *The APPEA Journal*, 26(1), 363–374. <https://doi.org/10.1071/aj85031>
- Wood, J. M., Sanei, H., Haeri-Ardakani, O., Curtis, M. E., Akai, T., & Currie, C. (2018). Solid bitumen in the Montney Formation: Diagnostic petrographic characteristics and significance for hydrocarbon migration. *International Journal of Coal Geology*, 198, 48–62. <https://doi.org/10.1016/j.coal.2018.09.004>
- Wood, R. E., & Ritzma, H. R. (1972). Analyses of oil extracted from oil-impregnated sandstone deposits in Utah. *Utah Geological Survey*. <https://doi.org/10.34191/SS-39>
- Xie, D., Yao, S., Cao, J., Hu, W., Wang, X., & Zhu, N. (2021). Diagenetic alteration and geochemical evolution during sandstones bleaching of deep red-bed induced by methane migration in petroliferous basins. *Marine and Petroleum Geology*, 127, 104940. <https://doi.org/10.1016/j.marpetgeo.2021.104940>
- Yoshida, H., Hasegawa, H., Katsuta, N., Maruyama, I., Sirono, S., Minami, M., et al. (2018). Fe-oxide concretions formed by interacting carbonate and acidic waters on Earth and Mars. *Science Advances*, 4(12), eaau0872. <https://doi.org/10.1126/sciadv.aau0872>
- Zaki, R., Wali, A., & Mosa, M. (2011). Sedimentological and hydrochemical spectrum of recent continental sabkha and signs of its capabilities to generate hydrocarbons: A case study in northwest El Fashn area, Western Desert, Egypt. *Carbonates and Evaporites*, 26(3), 273–286. <https://doi.org/10.1007/s13146-011-0062-5>